Published in final edited form as:

Cell Rep. 2025 March 25; 44(3): 115356. doi:10.1016/j.celrep.2025.115356.

Temporal dynamics of immune cell transcriptomics in brain metastasis progression influenced by gut microbiome dysbiosis

Samantha M. Golomb[1,2,3,4], **Ian H. Guldner**[3,4], **Emilija Aleksandrovic**[1,2,3,4], **Shaneann R. Fross**[1,2,3,4], **Xiyu Liu**[1,2,3,4], **Lu Diao**[1,2], **Karena Liang**[1], **Jinxuan Wu**[1], **Qingfei Wang**[3,4], **Jacqueline A. Lopez**[3], **Siyuan Zhang**[1,2,3,4,5,*]

[1]Department of Pathology, UT Southwestern Medical Center, Dallas, TX 75390, USA

[2]Harold C. Simmons Comprehensive Cancer Center, Dallas, TX 75390, USA

[3]Department of Biological Sciences, College of Science, University of Notre Dame, Notre Dame, IN 46556, USA

[4]Mike and Josie Harper Cancer Research Institute, University of Notre Dame, 1234 N. Notre Dame Avenue, South Bend, IN 46617, USA

[5]Lead contact

SUMMARY

Interactions between metastatic cancer cells and the brain microenvironment regulate brain metastasis (BrMet) progression. Central nervous system (CNS)-native and peripheral immune cells influence the BrMet immune landscape, but the dynamics and factors modulating this microenvironment remain unclear. As the gut microbiome impacts CNS and peripheral immune activity, we investigated its role in regulating immune response dynamics throughout BrMet stages. Antibiotic-induced (ABX) gut dysbiosis significantly increased BrMet burden versus controls but was equalized with fecal matter transplantation, highlighting microbiome diversity as a regulator of BrMet. Single-cell sequencing revealed a highly dynamic immune landscape during BrMet progression in both conditions. However, the timing of the monocyte inflammatory response was altered. Microglia displayed an elevated activation signature in late-stage metastasis in ABX-treated mice. T cell and microglia perturbation revealed involvement of these cell types in modulating BrMet under gut dysbiosis. These data indicate profound effects on immune response dynamics imposed by gut dysbiosis across BrMet progression.

In brief

---

[*]Correspondence: siyuan.zhang@utsouthwestern.edu.

AUTHOR CONTRIBUTIONS
S.M.G., I.H.G., and S.Z. conceived the original hypothesis and designed experiments. S.M.G., I.H.G., E.A., S.R.F., L.D., J.W., Q.W., J.A.L., and S.Z. performed experiments. S.M.G., X.L., K.L., and S.Z. analyzed data. S.M.G. and S.Z. wrote and revised the manuscript. S.Z. supervised the study. All authors reviewed the manuscript.

DECLARATION OF INTERESTS
The authors declare no competing interests.

SUPPLEMENTAL INFORMATION
Supplemental information can be found online at https://doi.org/10.1016/j.celrep.2025.115356.

With a multimodal time-course single-cell RNA sequencing analysis, Golomb et al. reveal dynamics of the brain immune environment in a mouse model of brain metastasis and the impact of gut microbiome dysbiosis. Gut dysbiosis is associated with increased brain metastasis outgrowth and changes in the immune response spanning different cell types.

Graphical abstract

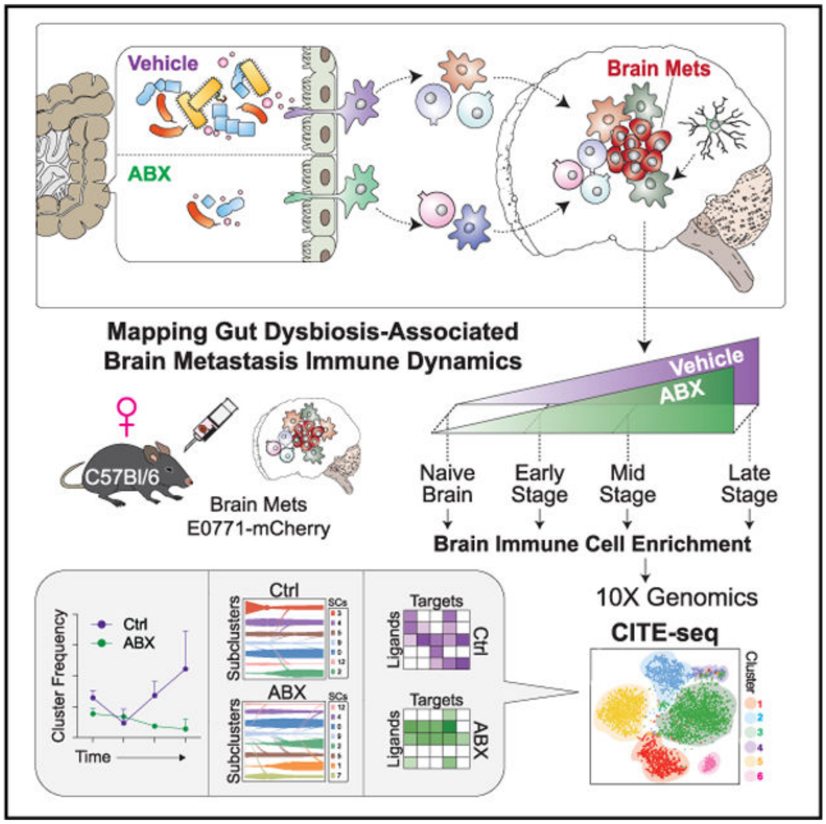

INTRODUCTION

Brain metastasis (BrMet) arises from complex interactions between tumor cells and factors in the tumor microenvironment (TME).[1,2] Astrocytes, endothelial cells, and immune cells, including CNS native and peripheral infiltrating, influence the success of BrMet.[2–8] Single-cell RNA sequencing (scRNA-seq) has revealed extensive immune cell heterogeneity in healthy and diseased CNS states.[6,7,9–12] However, the temporal dynamics of immune cells and the role of systemic factors modulating the potency, timing, and nature of the immune response remain unknown.

Systemic factors may reshape the BrMet TME, subsequently affecting therapeutic outcomes. The gut microbiome is a systemic factor that potently affects immune activity and has bidirectional communication with the brain.[13–16] The gut can communicate to the brain through direct engagement of gut microbiota-derived molecules with CNS-native immune cells.[17–19] The gut also indirectly regulates brain immunity through reprogramming of peripheral immune cells poised to respond to neuroinflammation.[20–23] Thus, alterations of the gut microbiome may influence CNS-native and peripheral immune responses across the metastatic cascade.

Here, we employed scRNA-seq to investigate the immune dynamics across BrMet progression in mice with and without gut dysbiosis. Gut dysbiosis was associated with increased BrMet burden at late-stage metastasis and differences in frequencies and transcriptomic signatures of immune cell subtypes. Perturbation of $CD3^+$ T cells and microglia revealed involvement of these cell types in modulating BrMet under gut dysbiosis.

RESULTS

Gut dysbiosis is associated with increased BrMet

To evaluate how gut dysbiosis impacts BrMet outgrowth, mice received a broad-spectrum antibiotic cocktail (ABX) including metronidazole, vancomycin, ampicillin, and neomycin or vehicle treatment before and during tumor outgrowth in an experimental model of BrMet (Figure 1A). After 14 days of ABX pre-treatment (14 day pre-tx), 16S rRNA-seq revealed significant changes in the gut microbiome composition and overall lower levels of diversity compared to vehicle-treated controls (Figures 1B, left, and S1A). At the endpoint (14 days post injection [dpi]), ABX-treated mouse ceca were enlarged with dark cecal content compared to vehicle-treated mice, as noted in previous reports using ABX and germ-free mice (Figure 1B, right).[17,24] Brain-seeking E0771 mCherry-tagged cells were injected into the carotid artery of adult female C57BL/6 hosts with or without gut dysbiosis (14 days post vehicle or ABX pre-tx). BrMet burden was significantly increased at 14 dpi (Figure 1C). Healthy body weight was maintained through the vehicle and ABX treatment course (Figure S1B).

To evaluate the dependency of increased BrMet burden on gut dysbiosis/diversity, we reconstituted the gut microbiome of ABX-pre-treated mice. Gut microbiome composition and diversity were equalized in vehicle- and ABX-pre-treated mice after co-housing and fecal matter transplantation (FMT) with fecal material retrieved from vehicle-pre-treated controls (Figure S1C). Restoration of a diverse microbiome in ABX-pre-treated mice was confirmed by 16S sequencing (Figures 1D, left; 1E; and S1D). Mouse cecum size and color were also phenotypically similar at the endpoint (Figure 1D, right). Alpha diversity was increased post FMT in both vehicle- and ABX-pre-treated groups (Figure 1E). FMT revoked the increased BrMet burden phenotype under gut dysbiosis, suggesting a regulatory role of microbiome diversity in BrMet progression (Figure 1F).

Short-chain fatty acids (SCFAs) are an abundant by-product of the gut microbiota and impact microglia function, T cell differentiation, and activation and are associated with colitis-induced colorectal cancer development.[17,25–29] SCFAs can inhibit histone deacetylases and modify immune cell functions through epigenetic remodeling.[25,30] We hypothesized that SCFA paucity in ABX-treated mice may significantly contribute to the ABX-associated increased BrMet burden. However, SCFA cocktail (sodium acetate, sodium butyrate, and sodium propionate) supplementation in ABX-treated mice did not significantly reverse the effect of gut dysbiosis on facilitating BrMet progression (Figures 1G and S1E).

SCFAs reshaped the composition of the immune milieu in infectious disease contexts.[31,32] In BrMet, the percentage of Ly6C$^{\text{Low}}$ patrolling monocytes was significantly increased within bone marrow-derived myeloid cells with SCFA supplementation (Figures 1H and S1F).

CITE-seq delineates dynamics of the brain immune environment in BrMet outgrowth in mice with and without gut dysbiosis

Gut dysbiosis disrupts homeostasis of the immune system and the brain immune environment.[16,17,33] Therefore, we hypothesized that gut dysbiosis would significantly disrupt the immune response to progressing BrMet. We profiled brain immune cells using cellular indexing of transcriptomes and epitopes by sequencing (CITE-seq). Immune cells were isolated for CITE-seq from tumor-naive mouse brains and at early (4 dpi), mid (8 dpi) and late (14 dpi) time points in our experimental BrMet model with and without ABX treatment (Figure 2A). Immune cells were enriched from digested brains at each time point (0, 4, 8, and 14 dpi) and stained with a panel of 31 Totalseq antibodies (antibody-derived tags, ADT) to evaluate surface-level protein expression in conjunction with mRNA and Hashtag Oligo antibodies to denote biological replicates (three biological replicates obtained per time point and condition) (Table S1).[34] Each dataset underwent quality control procedures and was merged and integrated into a single object using canonical correlation analysis (CCA) to account for any batch affects using the Seurat R package (v.5) (Table S1; Figures S1G and S1H).[35,36] Single cells were clustered by transcriptional similarities using a principal-component analysis-based approach and projected onto a two-dimensional plot by uniform manifold approximation and projection (UMAP) with the CCA integrated reduction (Figure 2B). Cells were grouped into 37 transcriptionally distinct clusters (Table S2). Additionally, cell identities were assigned by canonical surface marker-based gating utilizing expression levels of the CITE-seq antibodies (Figure S2). Cell IDs assigned via gating (called gated cell IDs) were projected onto the RNA-based cluster UMAP, showing general alignment of gated cell IDs with RNA-based clusters (Figure S3A). However, there was notable spreading of gated cell IDs into different RNA-based clusters, revealing transcriptional plasticity of immune cells that share a similar cell surface phenotype (Figure S3B).[37]

Cells assigned gated cell IDs were collapsed into 9 “broad groupings” with the following identification and gene expression: (1) CNS_Native (*Sall1*, *P2ry13*, and *Tmem119*), (2) Dendritic_Cell (*Cd74*, *H2-Eb1*, and *H2-Aa*), (3) Mono_Mac (*Ms4a6c*, *Ccr2*, and *Plac8*), (4) Neutrophil (*Lcn2*, *Ly6g*, and *Retnlg*), (5) B_Cell (*Vpreb3*, *Pax5*, and *Cd79a*), (6) Innate_Lymphoid (*Nkg7*, *Ncr1*, and *Klrb1c*), (7) T_Cell (*Lat*, *Themis*, and *Cd3e*), (8) CD45™, and (9) Unidentified_CD45$^+$ (Figures 2C and S3C). Between vehicle- and ABX-treated mice, these broad subtypes exhibited similar proportional changes across time (Figures 2D–2F; Table S3). The percentage of CNS_Native decreased in late-stage BrMet, which can possibly be attributed to increased peripheral immune cell infiltration.

Differentially expressed genes (DEGs) were also measured between time points (early-stage vs. naive, mid-stage vs. early-stage, and late-stage vs. mid-stage) for each broad immune subtype under each treatment condition. DEG magnitude varied across time points and between conditions (Figure 2G). The magnitude of gene upregulation in Mono_Macs was reduced in ABX-treated mice from naive to early-stage (~3-fold) and mid- to late-stage (~1.4-fold). However, gene downregulation was increased in ABX-treated mice at the same time points (~3-fold from naive to early-stage and ~2-fold from mid- to latestage). CNS_Native cells had a high magnitude of gene upregulation under both conditions from naive to early-stage; however, at mid- to late-stage, about twice as many genes were upregulated in ABX-treated mice. Neutrophils exhibited differences across all time points, notably a stronger response (~10-fold) in vehicle-treated mice from mid- to late-stage compared to ABX-treated mice. B_Cells had an approximately two times stronger response from naive to early-stage in ABX-treated mice but a lower response from mid- to late-stage. Overall, at a broad level, the immune response during BrMet is dynamic in cell composition and gene expression, both of which are altered with gut dysbiosis. Therefore, gut microbiome status may be critical in regulating the immune response during BrMet.

Ly6c2$^+$ monocyte response diverges with ABX treatment

Non-microglia myeloid (NonMGMyeloid) cell clusters were subset and separated into 13 RNA-based Seurat subclusters (SCs) with broad-level annotations determined by myeloid subtype marker genes (Figures 3A and S3D; Table S2). SC3, with high *Mrc1* expression, resembles CNS-native, border-associated macrophages (BAMs) (Figure S3D; Table S2).[11] SC3 BAMs were dominant among NonMGMyeloids in the naive brain but decreased proportionally across BrMet progression (Figure 3B; Table S3). *Ly6c2*$^+$ monocytes, SC5 and SC2, had divergent fluctuation across time and were significantly enriched in ABX-treated mice at mid- and late-stage, respectively (Figure 3C; Table S3). SC9, SC1, and SC8, however, had consistent dynamics across BrMet progression in both vehicle- and ABX-treated mice (Figure S3E; Table S3).

To visualize transcriptomic plasticity, we performed RNA velocity analysis.[38,39] Because the RNA velocity algorithm is based on transcriptional dynamics spanning a timescale of hours, RNA velocity was calculated on the NonMGMyeloid clusters at individual time points.[38] Represented by arrows showing direction and speed, the velocity dynamical model revealed predicted trajectories among the myeloid populations at mid-stage, where significant changes in cluster proportions were also observed (Figure 3D). The percentage of SC5 increased in the ABX-treated mice at mid-stage and showed a bifurcated predicted trajectory, with one trajectory moving toward inflammatory monocyte SC1 and SC2 and the other toward SC7 (Figure 3D). The percentage of SC7 increased slightly in ABX-treated mice by late-stage and had a more differentiated macrophage phenotype (*Adgre4*, *Ace*, and *Treml4*) (Figure S3F; Table S3).

RNA velocity identifies highly dynamic (“top likelihood”) genes with pronounced dynamic behavior.[39] Five top likelihood genes of SC5 (*Oasl1*, *Iigp1*, *Gbp2*, *Gbp5*, and *Nampt*) were also downregulated in ABX-treated mice (Figure S3G; Table S5). Highly dynamic genes potentially drive differentiation; thus, this reduced expression in Ly6C$^+$ monocytes in ABX-treated mice suggests divergence in the differentiation dynamics between conditions.[39] Next, we employed the CellRank 2 Real Time kernel, incorporating the multiomics single-cell optimal transport framework to evaluate cell trajectories across time points.[40] Visualized by plotting the probability mass flow by time in “vein” plots, SC5 cells were predicted to give rise to SC1 stronger from naive to early-stage (day 4) and early- to mid-stage (day 8) in vehicle-compared to ABX-treated mice (Figure 3E).[41] SC9 showed a divergent trajectory between conditions, with SC9 predicted to give rise toward SC1 from mid- to late-stage and SC2 from early- to mid-stage stronger in ABX-treated mice (Figure 3F).

Gene set variation analysis (GSVA) revealed that total Ly6C$^+$ monocytes (SC1, SC2, SC5, and SC9) in vehicle-treated mice were enriched in interferon (IFN) stimulation gene sets (e.g., response to IFNb and IFNII) and response to cytokine compared to ABX-treated mice at mid-stage (Figure 3G; Table S6). Conversely, by late-stage, expression of IFN and response to stimulation gene sets were enriched in ABX- compared to vehicle-treated mice (Figure 3H; Table S6). Of note, some gene sets down in ABX at mid-stage were enriched at late-stage (defense response to symbiont, cell killing, and response to IFNb), suggesting a potential delay in the Ly6C$^+$ response in ABX-treated mice (Figure 3H; Table S6). Some gene sets enriched in late-stage Ly6C$^+$ in ABX-treated mice were indicative of immune-regulatory programs to induce tolerance or minimize tissue damage (negative regulation of innate immune response and negative regulation of production of IFNII) (Figure 3H; Table S6).

Ifng$^+$ ILC1-like cells are candidate drivers of monocyte IFN response

Ly6C$^+$ monocytes exhibited an IFN response through upregulation of IFN response genes (*Gbp2*, *Gbp5*, *Oasl1*, *Irf1*, and *Ifi47*) and the Response-to-IFNb gene set (Figures 3G, 3H, and S3G; Tables S5 and S6). T_Cell and Innate_Lymphoid subtypes most dominantly expressed *Ifng* among total cells (all time points and conditions) (Figure S3H). Clusters with natural killer (NK) cell, innate lymphoid cell (ILC), and T cell transcriptional signatures were subset and reclustered into 13 SCs (Figure S4A). Conventional CD4 (*Cd4* and CITE-CD4) and CD8 (*Cd8a*, *Cd8b1*, and CITE-CD8a) T cells are comprised of SC1, SC5, SC10, and SC2 (Figure S4B; Table S2). SC6 and SC4 resemble innate-like T cells, γδ T (*Tcrg-C1* and *Trdv4*) and NK T cells (*Klra1* and *Klra6*), respectively. The remaining SCs resemble ILCs and NK cells annotated as NK-like (*Gzma*, *Prf1*, and *Ncr1*, SC0 and SC12), ILC1-like (*Styk1* and *Itga1*, SC3 and SC11), ILC2-like (*Gata3* and *Areg*, SC9), and ILC3-like (*Cd74* and *Gpx1*, SC7 and SC8) (Figure S4B; Table S2).[42] Within this subset, SC11 had highest expression of *Ifng* (Figure S4C). NicheNet analysis identified *Ifng* as the top-predicted SC11-derived ligand to drive gene expression changes in Ly6C$^+$ monocytes (Figure 3I).[43] Aligned with the asynchronous IFN response observed in monocytes (Figures 3G and 3H), *Ifng* was predicted to regulate the IFN response in monocytes specifically from early- to mid-stage metastasis in vehicle-treated (Figure 3I, left) and mid- to late-stage in ABX-treated mice (Figure 3I, right). Moreover, using *Ccr2*$^{-/-}$ mice, we evaluated the influence of peripheral monocytes in BrMet under ABX versus vehicle treatment conditions (Figure S4D). We observed a trend, but not a statistically significant increase, in BrMet outgrowth associated with ABX, suggesting that absence of *Ccr2* expression does not significantly obstruct the BrMet-promoting role of gut dysbiosis (Figure S4D). Notably, *Ccr2* expression was observed across other NonMGMyeloid SCs, suggesting that this observation is not specifically attributed to the Ly6C$^+$ monocyte population (Figure S4E).

TNF^{High} inflammatory microglia are enriched in late-stage BrMet in mice with gut dysbiosis

We subset microglia containing clusters and reclustered microglia into seven SCs (Figure 4A). The percentages of SC0 and SC3, expressing microglia homeostasis genes (*Cx3cr1*, *P2ry12*, *Tmem119*, and *Fcrls*) decreased at late-stage (Figures 4B and S4F), while the percentages of SC2 and SC5, expressing disease-associated microglia (daMG) signatures (daMG2, daMG3, and daMG4) increased (Figures 4B and 4C).[10,12,44] Upregulation of daMG genes overlapped between SC2 and SC5, but SC2 contained a higher proportion of cells with the daMG3 signature (*Tnf*, *Ccl4*, and *Il1a*) (Figure 4C). SC5 had higher expression of daMG2 (*Cd74*, *B2m*, and *Mpeg1*) and daMG4 (*Imt2b* and *Ctss*) genes but was also marked by abundant expression of IFN-stimulated genes (ISG^{High}) (Figures 4C and S4G). The percentage of SC5 (ISG^{High}) increased in ABX-treated mice at late-stage (Figure S4H; Table S3). The percentage of SC2 (tumor necrosis factor [TNF]^{High}) increased sharply from mid- to late-stage BrMet (Figure 4D; Table S3). Although a small fraction in the naive brain, the percentage of SC2 was higher in vehicle-treated mice; however, by late-stage, SC2 was significantly enriched in ABX-treated mice (Figure 4D; Table S3). SC2 was also marked by expression of other inflammatory proteins and chemokines (*Ccl2*, *Ccl3*, *Ccl4*, and *Il1b*) and genes associated with stage 2 disease-associated microglia (DAM) (*Axl* and *Lpl*) (Figure S4I; Table S2).[10] Overall, microglia with inflammatory signatures become the dominant microglia subpopulation at late-stage under gut dysbiosis and have a heightened inflammatory signature with enrichment of immune-related gene sets and ISGs (Figures 4E and 4F; Tables S3 and S6). Furthermore, GSVA across time points revealed that several immune-related gene sets were uniquely enriched in the ABX-treated mice (e.g., Response-to-IFNb and IL18-Production) (Figure S5A; Table S6).

ABX treatment alters microglia homeostasis

Microglia upregulate inflammatory signatures with neuroinflammation, making it challenging to determine gene expression changes attributed to gut dysbiosis concomitant with progressing BrMet.[5,10,12,45] We examined DEGs maintained in microglia from baseline (naive) across stages of BrMet outgrowth. Consistent DEGs between conditions from baseline through mid-stage were *Ccnd3*, *Btaf1*, *Fkbp5*, and *Ddit4*, which encode cellular processes, including regulation of transcription, the cell cycle, and protein folding/trafficking.[46–48] *Btaf1* was the only DEG across all time points (Figures S5B and S5C; Table S7). *Ddit4*, a marker gene of homeostatic SC0 and SC3, was a notable DEG in microglia from germ-free and ABX-treated mice (Table S7).[18] These consistent DEGs suggest that microglia may be poised for an altered response in ABX-treated mice compared to mice with an intact gut microbiome. Also, at mid- and late-stage metastasis, ribosomal and mitochondrial-ribosomal protein genes were significantly upregulated in microglia in ABX-treated mice (Figure S5D; Table S7). Increased ribosomal biogenesis may indicate that microglia are not only differentiating but also proliferating in response to progressing BrMet.[49] The presence of proliferating microglia was validated by Ki67 immunofluorescent staining (Figure S5E).

TNF^{High} microglia are predicted to be a differentiated subset of the microglia population

RNA velocity was calculated for the microglia subset at each time point to evaluate differentiation patterns. Inferred trajectories were consistent across early-, mid-, and late-stage, showing homeostatic microglia (SC0 and SC3) on a trajectory toward Tnf^{High} SC2 (Figures 4G, mid-stage only, and 4H). We evaluated whether any highly dynamic genes associated with mid-stage were also differentially expressed between ABX- and vehicle-treated mice (Table S7). *Dnajb1*, *Rsrp1*, and *Hspa8*, were highly dynamic genes at mid-stage and upregulated in microglia in ABX-treated mice (Figures 4I and S5F). With CellRank2, we observed cells in homeostatic SC0 and SC3 give rise across all other microglia SCs over time, but there was stronger flow from SC3 to SC2 and SC0 to SC2 at mid- to late-stage in ABX- compared to vehicle-treated mice (Figures 4J and 4K). This pattern, with the predicted trajectory dynamics toward SC2, suggests that homeostatic microglia may more strongly give rise to SC2 in ABX-treated mice, leading to the increased frequency at late-stage metastasis (Figure 4D).

T cells impact BrMet outgrowth under ABX conditions

Gut microbe-derived factors are partly responsible for maintaining T cell homeostasis.[25,50–52] Therefore, we evaluated the impact of gut dysbiosis on BrMet in the absence of an adaptive immune system. ABX-treated *B6.Rag1*$^{-/-}$ mice were associated with a significant decrease in BrMet burden versus vehicle-treated mice, contrary to the observation in wild-type (WT) mice (Figure 5A). Systemic depletion of CD3^{+} T cells using an anti-CD3 antibody (clone 145–2C11) during the ABX pre-tx phase (Figure S6A) also led to a significantly reduced BrMet burden under ABX treatment (Figure 5B). These data suggest that gut dysbiosis impacts the adaptive immune system and that, under ABX treatment, CD3^{+} T cells played a tumor-promoting role in BrMet outgrowth.

CITE-CD3^{+} SCs (SC1, SC2, SC4–SC7, and SC10) were subset (Figure S6B) and reclustered, revealing 13 CD3^{+} SCs that fluctuated in frequency across time (Figures 5C and 5D; Table S3). The percentage of CD3^{+} SC3 was significantly reduced in mice with gut dysbiosis in the naive brain and throughout later stages of BrMet outgrowth (Figure 5E; Table S3). CD3^{+} SC3 resembles *Il17a*$^{+}$ γδ T cells and shares marker genes (*Il17a*, *Trdv4*, *Cd163Ll1*, and *Blk*) with previously described meningeally resident interleukin (IL)-17a^{+} γδ T cells (Figure S6C; Table S2).[53] Significant TCRgd^{+} T cell depletion at late-stage BrMet in ABX-treated mice was confirmed in an independent cohort of mice by flow cytometry (Figure S6D). Also, TCRgd^{+} T cells were reduced in circulation while mice were in the ABX pre-tx phase, suggesting that gut dysbiosis causes a reduction in this population preceding BrMet induction (Figure 5F).

IL-1β stimulated IL-17 production and anti-tumor functions of γδ T cells in an immunogenic chemotherapy context.[54] Although *Il1b* expression is high in the BrMet niche under vehicle and ABX treatment conditions, *Il1b* expression did not rescue the *Il1r1*$^{+}$ γδ T cell population in the brain TME of ABX-treated mice (Figure S6E). The presence of *Il17a*$^{+}$ γδ T cells associated with decreased metastasis in the vehicle-treated group (reduced tumor burden) (Figure 5E) contrasting with other cancer contexts, where IL-17A^{+} γδ T cells promoted tumor development and metastasis through recruitment of neutrophils.[55,56] To evaluate a potential functional role of γδ T cells in BrMet, WT mice were systemically administered an anti-TCRgd antibody (clone UC7–13D5) or immunoglobulin G (IgG) isotype prior and during BrMet outgrowth (Figure S6F). Hindrance of receptor-ligand interactions with the γδ T cell receptor (TCR) was found to be dispensable during BrMet outgrowth (Figure 5G). Of note, this anti-TCRgd clone causes γδ TCR internalization and not γδ T cell depletion.[57] Therefore, we also evaluated IL-17A neutralization during BrMet. Systemic administration of an anti-IL-17A-neutralizing antibody (clone 17F3) the day before tumor cell injection and during BrMet outgrowth resulted in a trend decrease in tumor burden (Figure S6G). The significant depletion of *Il17a*$^+$ γδ T cells associated with gut dysbiosis is noteworthy, with previous studies finding roles for this cell type in other neuro-related conditions.[20,53] However, we found no significant role for the γδ TCR in BrMet progression in our model.

Predicted interaction partners of Tnf^{High} microglia

Activated microglia that downregulate *Cx3cr1* exerted BrMet-promoting effects through immune checkpoint mechanisms.[5] We assessed top-predicted ligands derived from TNF^{High} microglia (SC2) driving gene expression changes from mid- to late-stage metastasis in the CD3$^+$ T cells. In vehicle-treated mice, *Tgfa* and *Il1b* were top-predicted ligands to regulate a variety of genes and some transcription factors (*Fos*, *Jun*, *Nfkb1*, and *Stat5a*) from mid- to late-stage metastasis in CD3$^+$ T cells (Figure 5H, top). Ligand-receptor interaction analysis revealed less of a likelihood that CD3$^+$ cells received *Tgfa*-driven signals due to a lack of *Tgfa* receptor expression. However, *Il1b*-driven signaling had a greater likelihood with *Il12rb2* and *Il1rap* receptor expression (Figure 5H, bottom). *Tnf* was a top-predicted microglia SC2 ligand driving several gene expression changes in CD3$^+$ T cells in ABX-treated mice (Figure 5I, top). Others included *Il1b*, *Ebi3*, *Ccl5*, and *Il1a*, all with corresponding receptors present in CD3$^+$ T cells (Figure 5I, bottom). *Tnfrsf1a*, *Traf2*, and *Tnfrsf1b* receptors are expressed on CD3$^+$ T cell receivers with likely interaction with the *Tnf* ligand (Figure 5I, bottom).

Characterization of T cell targets of Tnf^{High} microglia

SC7, SC9, SC11, and SC12 exhibited higher and more abundant expression of *Tnf* receptors *Tnfrsf1b* and *Tnfrsf1a* relative to other CD3$^+$ SCs, suggesting that they may be targets of Tnf^{High} microglia (Figure 6A). Downstream target genes of TNF included transcription factors, *Fos*, *Irf1*, *Irf7*, and the nuclear factor κB family, all expressed in SC7, SC9, SC11, and SC12 (Figure 6B). SC7 was enriched in a CD4$^+$ regulatory T cell (Treg) signature with *Foxp3*, *Il2ra*, *Ctla4*, and *Pdcd1* expression as well as effector genes *Ccr8*, *Icos*, *Lag3*, and *Tnfrsf18* (glucocorticoid-inducer TNFR-related protein; GITR) (Table S2).[58] Cells in SC7 co-expressed TNF receptor and Treg markers, suggesting that CD4$^+$ Tregs may be poised for TNF-mediated signaling (Figure S6H). The percentage of CD4$^+$ Treg SC7 increased across BrMet progression and was slightly higher in ABX-treated mice (Figure 6C, left). SC9 and SC11 were a CD3^{Low} subset of ILC3-like cells expressing *Cd74*, *Gpx1*, *Cxcl2*, *Hk2*, *Lpin2*, and *Vegfa* (Figure S7A). CD3$^+$ SC11 frequencies were consistently higher in ABX-treated mice and, by late-stage, were significantly higher within CD3$^+$ ILC3-like cells (Figure 6C, right; Table S3).

Microglia depletion is associated with decreased BrMet and changes in T cell subtypes under ABX treatment

With increased TNF^{High} microglia in ABX-treated mice (Figure 4D), we evaluated the impact of microglia depletion (MGDep) on BrMet and the frequency of T cell populations under ABX treatment. Cx3cr1$^{CreERT/+}$:Rosa26$^{iDTR/+}$ transgenic mice and a temporally segregated tamoxifen and diphtheria toxin administration scheme were used to exclusively deplete microglia (Figures 6D and S7B).[5,59,60] Cx3cr1$^{CreERT/+}$ mice were used as non-depleted controls. Following cre-mediated recombination and a rest period for peripheral myeloid cell turnover, mice underwent ABX treatment and BrMet induction as described previously, with MGDep initiated at 4 dpi (Figure 6D, top). Mice with MGDep exhibited decreased BrMet, suggesting that microglia contribute a tumor-promoting role under gut dysbiosis (Figure 6D, bottom). Immune cells were enriched from the tumor-burdened brains for flow cytometry to assess CD4$^+$ Treg dependency on microglia. Although MGDep led to decreased BrMet, there was no change in the percentage of PD1$^+$CD4$^+$ Tregs (Figures 6E, left, and S7C). However, the percentage of PD1$^-$ Tregs was significantly decreased (Figures 6E, right, and S7C).

γδ T cells (CD3$^+$ SC3) were not predicted to be strong targets of inflammatory microglia SC2 (Figures 6A and 6B); however, within the CD3$^+$ population, the percentage of TCRgd$^+$ T cells was significantly increased in metastasis-burdened brains with MGDep under ABX treatment (Figure 6F). Next, we questioned whether the increased level of γδ T cells was driven by MGDep or was an accompanying phenotype with decreased tumor burden. In tumor-naive brains, the percentage of TCRgd$^+$ T cells increased with MGDep under both conditions (vehicle, $p = 0.014$; ABX, $p = 0.063$), but there were no significant changes in CD8$^+$ or CD4$^+$ T cells (Figures 6G–6I). This suggests that microglia play a role in specifically regulating γδ T cell levels in the CNS but not in a microbiome-dependent manner.

We also noted high interaction potential for microglia major histocompatibility complex class I (MHCI) ligands (classical, *H2-K1*; non-classical, *H2-Q4* and *H2-T23*) with *Cd8a* and killer cell Ig-like receptor genes (Figure 5I, bottom). We then assessed the impact of MGDep on the percentage of CD8, NK, and NK T cells expressing receptors for microglia MHCI ligands (Figures 7A and 7B; Table S2). We utilized surface markers, NKG2A (*Klrc1*) and CD107a (*Lamp1*), to evaluate changes in the percentage of CD8, NK, and NK T cells that may be impacted through interaction with the microglia MHCI ligand *H2-T23* (Figure S7D).[61–64] Within NKG2A$^+$ NK T cells, the percentage of NKG2A$^+$CD107a$^-$ cells was increased and the percentage of NKG2A$^+$CD107a$^+$ was decreased with MGDep (Figure 7C). CD8 and NK cells with and without NKG2A, CD107a, and PD1 expression had no significant changes (Figures 7D, 7E, and S7C). To glean functional differences between CD107a− and CD107a$^+$ NK T cells, *Klrc1*$^+$*Lamp1*$^-$ and *Klrc1*$^+$*Lamp1*$^+$ cells were subset from CD3$^+$ NK T cell SC2 in our single-cell data (Figure 7F). *Klrc1*$^+$*Lamp1*$^+$ NK T cells were enriched in the granzyme-mediated cell death pathway, indicating an enhanced cytotoxic function compared to *Klrc1*$^+$*Lamp1*$^-$, as well as autophagic cell death and Golgi to lysosome transport pathways (Figure 7G; Table S6).

DISCUSSION

The brain immune landscape diversifies significantly with the onset of BrMet. Immune dynamics critically regulate tumor progression and vary among patients, influencing BrMet susceptibility and outcomes. Therefore, understanding these dynamics and the influence of systemic factors, like the gut microbiome, is essential for developing novel and effective therapeutics.[13,65] Leveraging gut microbiome dysbiosis as a model, we investigated how systemic immune perturbation influences BrMet and the immune response.

Brain TME complexity encompasses major regulators and immune modulators of metastasis

This study highlights how gut dysbiosis potentiates BrMet through alterations of the immune cell responses. Peripherally-derived monocytes, CNS-resident microglia, and $\gamma\delta$ T cells were impacted, and perturbation experiments revealed varying levels of their regulatory roles in the brain TME. CD3$^+$ T cell depletion and MGDep significantly altered tumor outgrowth (Figure 6), *Ccr2*$^{-/-}$ and anti-IL17A had moderate yet consistent trends (Figures S4 and S6), and anti-TCRgd had a negligible impact (Figure 5). Perturbations with moderate influence should not be dismissed due to lack of statistical significance and, rather, be regarded as insights into the complex interconnected functions among brain TME cells. For example, lack of statistical significance for CCR2 and IL-17A perturbations does not necessarily negate their regulatory roles but, rather, suggests their involvement as part of a network of redundant mechanisms. Our findings demonstrate that functional redundancy exists within the brain TME, enabling metastatic tumors to adapt and persist even when individual pathways are disrupted.[66] This inherent robustness of immune regulation poses a significant challenge in resolving signaling networks supporting cancer progression. The profiling data generated here may provide a foundation for future studies aimed at dissecting these mechanisms.

Microglia are critical regulators in the BrMet immune TME

Microglia have been implicated previously in regulating BrMet, but their role remains incompletely understood, as evidenced by reports suggesting both tumor-promoting and tumor-suppressing capabilities.[5,45] Microglia had a significant impact on BrMet under gut dysbiosis and exhibited dynamic transcriptomic changes across tumor progression (Figures 4 and 6). Given these changes across time, it is plausible that microglia exert tumor-suppressing and -promoting forces in the TME depending on the stage of tumor outgrowth. Under gut dysbiosis, we identified immune cell types within the TME network that are seemingly impacted by microglia (PD1$^-$ Tregs, NK T cells, and $\gamma\delta$ T cells), which may collectively influence later stages of BrMet. Uncovering these cellular networks may further identify intercellular communication in the TME and the influence on tumor growth.

Notably, the percentage of $\gamma\delta$ T cells increased in the CNS with MGDep and was associated with decreased BrMet under gut dysbiosis, suggesting that MGDep may have rescued the $\gamma\delta$ T cell population (Figure 6F). Given the complexity of the TME, the changes in $\gamma\delta$ T cells with MGDep may reflect contributions from diverse signals originating from microglia, infiltrating immune cells, and alterations in the TME resulting from MGDep.

Interestingly, the same phenomenon in tumor-naive brains with and without ABX suggests that microglia-derived signals regulate γδ T cells in the CNS at homeostasis (Figure 6H). Future investigations will be valuable given previous findings demonstrating physiological roles of γδ T cells in brain function and behavior.[53]

Microbiome perturbation reveals a gut-brain connection in BrMet-induced neuroinflammation

Through this profiling, it is evident that gut dysbiosis impacts numerous aspects of the immune response that likely collectively contribute to the changes in BrMet. But how are gut microbes influencing the changes we see in the immune cell response? Numerous publications have demonstrated that whole FMT, microbial consortia, or different metabolites can elicit a range of anti-cancer effects and influence immune cell functions.[67–70] Given the heterogeneity of cancer and accompanying immune responses, we believe it is likely that our observed phenotype arises from a network of microbiota-derived signals rather than a single microbial strain or metabolite. Leveraging the gut microbiota to enhance immunotherapy is appealing due to the minimally invasive nature of microbiome modulation, though identifying optimal microbial consortia remains challenging.[71] As the field continues to examine the gut-cancer axis, integrating gut-brain studies will advance our understanding of the complex interplay between systemic and brain-specific immune responses.

In summary, this study characterizes the dynamic nature of the immune response during BrMet outgrowth and illuminates how this response is impacted by gut microbiome dysbiosis. Our findings necessitate the need to better understand implications of gut microbiome composition and use of ABX in patients susceptible to BrMet relapse.

Limitations of the study

This study focused on one model of BrMet and gut dysbiosis, limiting these findings to be specifically attributed to the cell line, mouse models, and ABX treatment used here. Future work will ideally explore other models of BrMet and gut dysbiosis, such as germ-free mice.

Despite employing a precise means of tumor cell injection by intra-carotid injection for modeling BrMet, we observed significant biological variability potentially masking subtle phenotypes. We believe that the variability is likely due to (1) the stochastic nature of tumors seeding in different brain regions and (2) altered pressure from diverse TMEs across different genetic backgrounds and immune cell perturbations.

Additionally, the broad-spectrum ABX cocktail used throughout this study does not mimic clinical scenarios. In our study, this approach was chosen as a method of experimental gut dysbiosis based on prior studies identifying microbiota-brain immune crosstalk.[17] Future pre-clinical investigations with a focus on optimizing anti-cancer therapeutics with or without ABX treatment for clinical applications should employ clinically translatable ABX strategies.

RESOURCE AVAILABILITY

Lead contact

Requests for further information and resources should be directed to lead contact, Siyuan Zhang (siyuan.zhang@utsouthwestern.edu).

Materials availability

This study did not generate new unique reagents.

Data and code availability

- CITE-seq and 16S data were deposited at GEO and are publicly available as of the date of publication. Accession numbers are listed in the key resources table.
- Code used to analyze data is available upon request from the lead contact.
- Microscopy data reported in this paper are available from the lead contact upon request.
- Additional information required to reanalyze the data reported in this paper is available from the lead contact upon request.

STAR★METHODS

EXPERIMENTAL MODEL AND STUDY PARTICIPANT DETAILS

Mice—All animal studies were performed ethically and in accordance with IACUC protocol approved by the University of Notre Dame and UT Southwestern Medical Center IACUC committees. C57BL/6 (000664), B6.129P2(Cg)-Cx3cr1$^{tm2.1(cre/ERT2)Litt/WganJ}$ (021160/Cx3cr1CreERT), C57BL/6-Gt(ROSA)26^{Sortm1}(HBEGF)$^{Awai/J}$ (007900/ROSA25iDTR), B6.129(Cg)-Ccr2$^{tm2.1Ifc/J}$ (017586/Ccr2$^{-/-}$) and B6.129S7-Rag1^{tm1Mom}/J (002216; B6.Rag1$^{-/-}$) mouse lines were purchased from Jackson Lab (Ben Harbor, ME). We produced Cx3cr1CreERT/+:R26iDTR/+ double transgenic mice in-house by breeding Cx3cr1CreERT with ROSA26iDTR mice. Cx3cr1CreERT/+ mice, used as controls in microglia depletion experiments, were produced in-house by breeding Cx3cr1CreER mice to C57BL/6 mice. Mice were bred and maintained by Friemann Life Science Center (FLSC) at the University of Notre Dame and the Animal Resource Center (ARC) at UTSW, with the exception C57BL/6, which were purchased from Jackson Lab. Mice purchased from Jackson Lab were acclimated for a minimum of 2 weeks in FLSC or ARC prior to experimental use. All mice used in experiments were females for modeling breast cancer brain metastasis and aged 2 to 6 months.

Cell lines & generation of experimental brain metastases—E0771 cell line (female origin) was purchased from CH3 Biosystems (Amherst, NY, 940001-Vial). Brain seeking E0771 (E0771.Br) cells were generated through one round of *in vivo* selection for cells with brain tropism. The E0771.Br cells were subsequently labeled with mCherry by lentiviral transduction. E0771 cells were cultured in RPMI media with 10% FBS and 1% Penicillin/Streptomycin and incubated at 37C, 5% CO_2 and humidity ~95%. E0771 cells were tested and found negative for mouse pathogens by IDEXX BioResearch

Inc. (IMPACT IV panel: PCR evaluation for: LCMV, MHV, MPV, MVM, Mycoplasma pulmonis, Mycoplasma sp., PVM, Sendai, TMEV). CellCheckTM Mouse Plus service provided by IDEXX BioResearch Inc. was used to track genetic drifting and potential cell line cross-contamination. Brain metastases were generated by injection of 3×10^5 cells into the left internal carotid artery.

METHOD DETAILS

ABX treatment—10-weeks old SPF C57BL/6 mice were purchased from Jackson Laboratory. Mice were acclimated in the animal facility for 2 weeks and randomized to normalize the gut microbiota. 12-weeks old mice were assigned either vehicle or antibiotics (ABX) treatment groups. The ABX groups received an ABX cocktail containing metronidazole (MedChem Express, 0.25 g/L), vancomycin hydrochloride (MedChem Express, 1 g/L), neomycin (VWR, 1 g/L), and ampicillin sodium salt (Fisher Scientific, 0.5 g/L). Vehicle or ABX was delivered by oral gavage every day for one week along with vehicle in cage bottles to acclimate mice to new water. In the second week of treatment, oral gavage occurred every other day and the ABX group received the ABX water in cage bottles. Oral gavage ceased after cancer cell injection but mice remained on vehicle or ABX treatment *ad libitum* via cage bottles. Mice were weighed every 3–4 days during treatment to check that healthy body weight was maintained. Fresh ABX cocktail was prepared every 2–3 days for oral gavage and cage bottle refill. Cages and water bottles were refreshed every 3–4 days to maintain a relatively clean environment inside the ABX treatment cages. Mouse stool samples were collected at days -14 (pre-treatment) and 0 (post-treatment prior to cancer cell injection).

Fecal matter transplant (FMT)—10-weeks old SPF C57BL/6 mice were purchased from Jackson Laboratory. Mice were acclimated in the animal facility for 2 weeks and randomized to normalize the gut microbiota. 12-weeks old mice were assigned into either vehicle pre-treatment or antibiotics (ABX) pre-treatment groups. Mice were pre-treated for 14 days with vehicle or ABX in the same manner as described above. Following the 14-day pre-treatment, all mice were switched to regular water and received PBS via oral gavage for a 2-day washout period. Next, mice from vehicle and ABX pre-treatment groups were randomized and cohoused. For FMT, fresh fecal pellets were collected from mice in the vehicle pre-treatment group. 2–3 pellets were placed in 1 mL of sterile PBS in a 1.5 mL tube and vortexed into a homogenate. The homogenates were then centrifuged at 500 g for 5 min and supernatant was collected. All mice received 200 μL of fecal matter supernatant by oral gavage. This procedure was repeated every other day for a seven-day period. Mice remained cohoused and on regular water following cancer cell injection. Mouse stool was collected at day -23 (pre-treatment), -9 (post-treatment), 0 (post FMT/cohouse) and 14 (endpoint) for 16S rRNA analysis.

Short chain fatty acid (SCFA) supplementation—10-weeks old SPF C57BL/6 mice were purchased from Jackson Laboratory. Mice were acclimated in the animal facility for 2 weeks and randomized to normalize the gut microbiota. 12-weeks old mice were assigned into either control or SCFA groups. The control group received the ABX cocktail described above supplemented with sodium and pH adjusted to match the water delivered in the SCFA group. The SCFA group received the ABX cocktail described above supplemented with sodium propionate (Sigma-Aldrich, 25 mM), sodium butyrate (Sigma-Aldrich, 40 mM) and sodium acetate (MP Biomedicals, 67.5 mM).[28] Control or SCFA cocktails were delivered in cage water bottles and by oral gavage once per day for one week and once every other day in the second week prior to cancer cell injection. Following cancer cell injection, mice continued to receive control and SCFA by oral gavage once per day until experiment endpoint (14 dpi). ABX and SCFA cocktails were prepared and placed in clean water bottles every 2–3 days.

***In vivo* antibody treatments—**For *in vivo* $CD3^+$ cell depletion, mice were treated with 200 µg of anti-CD3e (BioXCell, BE0001–1) or 200 µg of IgG isotype control (BioXCell, BE0091) two times per week in the 14-day ABX pre-treatment phase. For *in vivo* TCRgd blockade, mice were treated with 200 µg of anti-TCRgd (BioXCell, BE0070) or 200 µg of IgG isotype control (BioXCell, BE0091) two times in the week prior to tumor cell injection and two more times in the following two weeks post tumor cell injection. For *in vivo* IL-17A neutralization, mice were treated with 50 µg of anti-IL-17A (BioXCell, BE0173) or 50 µg of IgG isotype control (BioXCell, BE0083) the day before tumor cell injection and then every 3 days for the duration of brain metastasis outgrowth (two weeks post tumor cell injection). All antibody treatments were intended for systemic depletion/blockade and were administered by intra-peritoneal injection.

***In vivo* CNS myeloid depletion—**To achieve CNS resident myeloid cell depletion, 6–8 weeks old Cx3cr1CreERT/+ (control) and Cx3cr1CreERT/+:R26iDTR/+ mice were administered 100 mg/kg Tamoxifen (Sigma, T5648) dissolved in corn oil (Sigma, C8267) by intraperitoneal injection once daily for 4 consecutive days to induce genetic recombination. Mice were then rested for ~10.5 weeks prior to ABX pre-treatment followed by tumor cell injection 14 days later. Mice were administered 1 µg of Diphtheria Toxin (Sigma, D0564) dissolved in 100 µL of sterile saline by intraperitoneal injection every other day beginning at 4 days post-tumor cell inoculation.

16S rRNA sequencing and analysis—16S rRNA sequencing was performed on mouse stool samples in the same manner at both the University of Notre Dame Genomics & Bioinformatics Core Facility (ND GBCF) and the UT Southwestern Microbiome Core Facility (UTSW). Mouse fecal DNA extraction was performed using the ZymoBIOMICS DNA Miniprep Kit (Cat# D4300). 16S V3/V4 region amplification, sample indexing and library preparation were performed following the Illumina 16S Metagenomic Sequencing Library Preparation (PN 15044223 Rev. B). Amplicons sequenced at ND GBCF were indexed using the Nextera XT Index Kit (FC-131–1096). Amplicons sequenced at UTSW employed Illumina dual indexing. Both sequencing cores (ND GBCF and UTSW) normalized and multiplexed the libraries into a single pool prior and performed QC validation prior to sequencing. Libraries were sequenced on the MiSeq System using MiSeq V2 500 cycle kit (250-PE with 8-bp dual indexing) at ND GBCF and MiSeq 300 PE at UTSW. Base calling and demultiplexing were performed by MiSeq Controller Software. Divisive Amplicon Denoising Algorithm version 2 (DADA2) R package to analyze the 16S amplicon reads and construct the amplicon sequence variant (ASV) table. This package incorporates a quality-aware model of Illumina amplicon errors to improve the identification of real variants and minimize false positives.[77] DADA2 utilizes the Silva taxonomic database: https://doi.org/10.5281/zenodo.3986799.

Tissue collection and single cell preparation—For isolation of brain tissue and brain immune cells for flow cytometry or single cell RNA sequencing, mice were anesthetized with isoflurane and transcardially perfused with cold 1X PBS. Brain tissue used for immunofluorescence was placed in cold 4% paraformaldehyde for up to 4 h and subsequently moved through a gradient of sucrose solutions (15% followed by 30%). Brain tissues were embedded in Tissue-Tek Optimal Cutting Temperature (OCT) compound (Sakura, 4583) and snap frozen with isopentane at −20C.

For flow cytometry or single cell RNA sequencing, brain immune cell enrichment was performed as described in Guldner et al.[34] Briefly, brains were mechanically dissociated with scissors and triturated with a P1000 micropipet followed by enzymatic digestion with the Multi-tissue Dissociation Kit I (Miltenyi Biotec, 130-110-201). Immune cells were enriched from other neural cells through Percoll gradient centrifugation. The Percoll gradient and density layering were prepared (from bottom to top: 70%, 37%, 30%). Density gradient centrifugation was performed for 20 min at 2000rpm with no break. Mononucleated cells were isolated from the buffy layer between the interface of the clear Percoll and red-colored Percoll. Isolated cells were washed in 1X HBSS and the resultant cell suspension was processed as required for CITE-seq or flow cytometry.

For peripheral blood mononuclear cells (PBMCs) isolation, blood samples were withdrawn from anesthetized mice through the retro-orbital vein using a heparin-lined capillary tube. For splenocyte isolation, mice were sacrificed, and spleens immediately dissected. Spleens were mechanically dissociated using a 1 mL syringe plunger and cells were isolated through a 70 μm cell strainer. Red blood cells were lysed from blood and splenocyte suspensions with 1X red blood cell lysis buffer (Tonbo, TNB-4300-L100). Lysis buffer was neutralized with 1X PBS and PBMC and white blood cells were subsequently prepared for flow cytometry.

CITE-seq antibodies and cell staining—Following gradient centrifugation for brain immune cells enrichment, samples were prepared for 10X Genomics Chromium Single Cell Gene Expression analysis as described in the CITE-seq and cell hashing protocol on the CITE-seq website (https://citeseq.files.wordpress.com/2019/02/cite-seq_and_hashing_protocol_190213.pdf). Briefly, samples were blocked by incubation with FcR Blocking Reagent (Miltenyi Biotec, 130-092-575) in a 50 μL cell staining buffer for 20 min on ice. After blocking, samples were stained with Total-seq antibodies purchased from BioLegend: CCR2/CD192 (SA203G11, 150625), CD117/c-kit (2B8, 105843), CD11c (N418, 117355), CD172a/SIRPα (P84, 144033), CD38 (90, 102733), CD44 (IM7, 103045), CD45R/B220 (RA3–6B2, 103263), CD8a (53–6.7, 10073), CD90.1 (OX-7, 202547), Cx3cr1 (SA011F11, 149041), F4/80 (BM8, 123153), I-A/I-E (M5/114.15.2, 107653), Ly6C (HK1.4, 128047), Ly6G (1A8, 127655), NK1.1 (PK136, 108755), PD-1 (RMP1–30, 109123), PD-L1 (MIH6, 153604), CD169/Siglec-1 (3D6.112, 142425), Siglec-H (551, 129615), TMEM119 (A16075D, 853303), XCR1 (Zet, 148227), CD24 (M1/69, 101841), CD103 (2E7, 121437), CD64 (X54–5/7.1, 139325), CD83 (Michel-19, 121519), CD45 (30-F11, 103159), Cd11b (M1/70,101265), CD86 (GL-1, 105047), CD3 (17-A2, 100251), CD4 (RM4–5,100569), and CD25 (PC61, 102055). Additionally, each sample was stained with one unique hashing antibody purchased from BioLegend: HTO1 (M1/42; 30-F11, 155801), HTO2 (M1/42; 30-F11, 155803), HTO3 (M1/42; 30-F11, 155805), HTO4 (M1/42; 30-F11, 155807), HTO5 (M1/42; 30-F11, 155809) and HTO6(M1/42; 30-F11, 155811). After 25 min of staining, samples were washed 4 times prior to delivering the prepared samples to the ND GBCF for loading on the 10X Genomics Chromium Controller.

CITE-seq library preparation and illumina sequencing—ND GBCF prepared cells for 10X Genomics Chromium single cell capture and cDNA libraries according to the standard CITE-seq (https://citeseq.files.wordpress.com/2019/02/cite-seq_and_hashing_protocol_190213.pdf) and 10X Genomics standard protocols. Kits necessary for library preparation included Chromium Single Cell 30 Library and Gel Bead Kit v3 (10x Genomics, PN-10000092); Chromium Next GEM Single Cell 30 GEM Library and Gel Bead Kit v3.1 (10x Genomics, PN-1000121); Chromium Chip B Single Cell Kit (10x Genomics, PN-1000074); Chromium i7 Multiplex Kit (10x Genomics, PN-120262). Primers required for library preparation include:

ADT_TruSeq_i7_UDI01: CAAGCAGAAGACGGCATACGAGAACCGCGGGTGACTGGAGTTCCTTGGCACCCGAGAATTCCA.

HTO_Nextera_i7_UDP01: CAAGCAGAAGACGGCATACGAGATCGCTCAGTGTGACTGGAGTTCAGACGTGTG.

ADT-RPI-2: CAAGCAGAAGACGGCATACGAGATCGTGATGTGACTGGAGTTCCTTGGCACCCGAGAATTCCA.

HTO_Nextera_i7_UDP01: CAAGCAGAAGACGGCATACGAGATCGCTCAGTGTGACTGGAGTTCAGACGTGTG.

ADT_TruSeq_i7_UDI04: CAAGCAGAAGACGGCATACGAGTTGGACTTGTGACTGGAGTTCCTTGGCACCCGAGAATTCCA.

HTO_ Nextera_i7_UDP02: CAAGCAGAAGACGGCATACGAGATTATCTGACGTGACTGGAGTTCAGACGTGTGC.

ADT-RPI-1: CAAGCAGAAGACGGCATACGAGATCGTGATGTGACTGGAGTTCCTTGGCACCCGAGAATTCCA.

HTO-N701: CAAGCAGAAGACGGCATACGAGATTCGCCTTAGTGACTGGAGTTCAGACGTGTGC cDNA-, ADT-, and HTO-derived libraries were validated by Qubit High Sensitivity ds DNA and Agilent Bioanalyzer DNA HighSensitivity Chip assays. After which, libraries were submitted to Indiana University School of Medicine Center for Medical Genomics for multiplexing into a single pool and Illumina sequencing on a NovaSeq6000.

Flow cytometry cell staining—Following gradient centrifugation for brain immune cell enrichment or RBC lysis for PBMC and white blood cell isolation from splenocytes, cell suspensions were washed in homemade cell staining buffer (5% FBS, 0.1% NaN_3, 2mM EDTA in 1X PBS) in preparation for flow cytometry. For experiments utilizing viability dye, cells were stained using the ZombieAqua Fixable Viability Kit (BioLegend, 423102) (1000X diluted stock) at room temperature (RT) in the dark for 20 min. Following viability stain, cells were blocked in the same manner as described for CITE-seq preparation, using FcR Blocking Reagent (Miltenyi Biotec, 130-092-575) and then stained with one or a combination of the following antibodies: rat anti-mouse CD3e-647 (BioLegend, 155609, KT3.1.1), hamster anti-mouse TCR γ/δ-PE (BioLegend, 118107, GL3), rat anti-mouse CD117(c-kit)-PE-Cy7 (BioLegend, 105813, 2B8), mouse anti-mouse CX3CR1–421 (BioLegend, 149023, SA011F11), rat anti-mouse CD192(CCR2)-510 (BioLegend, 150617, SA203G11), rat anti-mouse CD3-SparkBlue550 (BioLegend, 100259, 17A2), rat anti-mouse CD8-FITC (BioLegend, 100706, 53–6.7), rat anti-mouse CD4–711 (BioLegend, 100549, RM4–5), rat anti-mouse Ly-6C-785 (BioLegend, 128041, HK1.4), rat anti-mouse Ly-6G-650 (BioLegend, 127641, 1A8), rat anti-mouse CD186(CXCR6)-PerCP/Cyanine5.5 (BioLegend, 151120, SA051D1), rat anti-mouse CD11b-605 (BioLegend, 101237, M1/70), rat anti-mouse CD45-PacificBlue (BioLegend, 103125, 30-F11), rat anti-mouse CD45-PerCP/Cyanine5.5 (BioLegend, 103131, 30-F11), rat anti-CD3-FITC (BioLegend, 100203, 17A2), hamster anti-mouse TCR γ/δ-PE-Cy7 (BioLegend, 118123, GL3), rat anti-mouse CD279(PD-1)-421 (BioLegend, 135217, 29F.1A12), rat anti-CD25-PE (BioLegend, 102007, PC61), rat anti-CD4-APC-Cy7 (Tonbo, 25-0042-U025, RM4–5), rat anti-mouse CD8a-710 (Tonbo, 80-0081-U025, 53–6.7), rat anti-mouse CD3-PacificBlue (BioLegend, 100213, 17A2), rat anti-mouse CD4–570 (BioLegend, 100541, RM4–5), rat anti-mouse CD8a-APC-Cy7 (BioLegend, 100713, 53–6.7), hamster anti-mouse TCR γ/δ−711 (BioLegend, 118149, GL3), mouse anti-mouse NK-1.1-SparkRed718 (BioLegend, 156533, S17016D), rat anti-mouse CD25–750 (BioLegend, 102077, PC61), mouse anti-mouse CD159a(NKG2A^{B6})-PE (BioLegend, 142803, 16A11), rat anti-mouse CD107a(LAMP-1)-PE-Cy7 (BioLegend, 121619, 1D4B), rat anti-mouse/human CD11b-650 (BioLegend, 101259, M1/70), rat anti-mouse CD8a-647 (BioLegend, 100727, 53–6.7), rat anti-mouse CD279(PD-1)-421 (BioLegend, 135221, 29F.1A12), rat anti-mouse FOXP3–647 (BioLegend, 126407, MF-14).

After staining, cells were washed with cell staining buffer. For experiments involving intra-cellular staining, cells were fixed for 1 h at room temperature in the dark using the True-Nuclear Transcription Factor Buffer Set (BioLegend, 424401) and resuspended in CytoLast (BioLegend, 422501) for overnight storage in the dark at 4C. The following morning, cells were permeabilized using the True-Nuclear Transcription Factor Buffer Set (BioLegend, 424401) and stained with rat anti-mouse FOXP3–647 (BioLegend, 126407, MF-14). After staining, cells were washed and resuspended with cell staining buffer and run on either a Beckman Coulter FC500 or Cytek Northern Lights.

Tissue immunofluorescence—Frozen brain cryosections were adhered to Superfrost Plus slides (Fisherbrand, 1255015), thawed at RT for 10–20 min and washed with 1X PBS to rehydrate and remove surrounding OCT. Tissues were then blocked with 5% donkey serum in TBST for 30 min at RT and stained with guinea pig anti-TMEM119 (Synaptic Systems, polyclonal, 400–004) overnight at 4C in a humidifying chamber. After overnight incubation, slides were washed three times, 5 min each, with TBST and then stained with Alexa Fluor 594 AffiniPure Donkey Anti-Guinea Pig IgG (H + L) (Jackson Immuno Research, 706-585-148) or Alexa Fluor 488 AffiniPure Donkey Anti-Guinea Pig IgG (H + L) (Jackson Immuno Research, 706-545-148) for 3 h at RT in a humidifying chamber. After incubation, slides were washed three times in TBST, stained with DAPI (Biotium, 40043) for 5 min at RT and washed again three times in TBST. After washing, coverslips were mounted onto the slides with Fluoromount-G mounting media (Electron Microscopy Sciences, 17984–25).

Microscopy—Fluorescent imaging of 10 μm thick brain sections was performed on a Nikon Ti2 inverted microscope. Images were captured in the same brain regions at 20× magnification with the same laser and exposure settings. Gross images of whole brains were acquired on a Leica M165 FC fluorescence stereoscope.

QUANTIFICATION AND STATISTICAL ANALYSIS

Metastasis burden—With a fluorescence stereo microscope (Leica M165 FC), mCherry+ macro-metastatic lesions in the brain were counted manually immediately upon PBS perfusion and brain extraction at experiment endpoints. Tumor numbers were analyzed for statistical significance using a two-tailed Student’s t test and outliers identified through Grubb’s test. p values <0.05 were considered statistically significant. Statistical analyses were performed and data were plotted with GraphPad Prism (GraphPad Software). Brain tumor counts were not performed blinded. Statistical tests, graph plotting details and number of replicates are described in figure legends for corresponding panels showing brain metastasis burden.

Immunofluorescent image analysis—Analysis for microglia depletion experiments was performed on immunostained brain sections by quantification of TMEM119+ area using the particle tool in FIJI.[72] Statistical significance was measured using a two-tailed Student’s t test and performed and visualized using GraphPad Prism (GraphPad Software). p values <0.05 were considered statistically significant. Image analyses were not performed blinded. Statistical tests, graph plotting details and number of replicates are described in the figure legend for corresponding panels with immunofluorescent staining.

Flow cytometry—Flow cytometry data were gated and analyzed using FlowJo software. Flow cytometry data was analyzed with Student’s t test and p values <0.05 were considered statistically significant. Statistical analyses were performed and data were plotted using GraphPad Prism. Flow cytometry analyses were not performed blinded. Statistical tests, graph plotting details and number of replicates are described in the figure legends for corresponding panels with flow cytometry data.

CITE-seq analysis—Raw FASTQ files were processed through CellRanger 7.2 (10x Genomics) for RNA, ADT and HTO expression matrices. For each timepoint (Day 0 (naive brain), Day 4 (early-stage), Day 8 (mid-stage) and Day 14 (late-stage), six HTOs were used to label three biological replicates per condition (vehicle and ABX). Each time point containing six HTOs was prepared into its own sequencing library, making four libraries (datasets) in total. Quality measures from CellRanger are detailed in Table S1. To account for any batch affects, single cell data collected from different time points (batches) were merged and integrated following the Seurat v5 integration workflow utilizing the anchor-based canonical correlation analysis (CCA) integration method.[36] Prior to merging, HTO (sample ID) expression data for each dataset was normalized and quality control (QC) was performed on individual datasets (batches) to subset out high-quality singlets. Each dataset was filtered to contain singlets with <5% mitochondrial genes (Figure S1H). Day 0, 4 and 8 datasets were filtered to contain singlets expressing 200–6500 genes, while Day 14 threshold was increased to include up to 10,000 genes to include tumor cells that were acquired (Table S1). QC-ed datasets were then merged and integrated. RNA expression data was normalized via SCTransform and ADT expression data normalized by centered-log ratio (CLR). Cells were demultiplexed to their original sample groups using the Cell Hashing tags (HTOs). Dimensional reduction, clustering and differential expression analyses were performed using the R Studio and R package, Seurat.[73,74] Dimensionality reduction by principal component analysis and UMAP embedding was performed for cell cluster visualization utilizing the integrated CCA reduction. Details about Seuratv5 and dimensionality reduction techniques can be found at: https://satijalab.org/seurat/. CITE-seq expression data was analyzed using Wilcoxon rank-sum test and adjusted p values <0.05 were considered statistically significant. GSVA was performed on subsets of cells from the final merged object.[75] Gene sets considered were obtained from the mouse M5 Gene Ontology Bioprocess database (https://www.gsea-msigdb.org/). Gene set expression data was merged with corresponding subset Seurat objects and analyzed using Seurat. Immune-related gene sets were filtered in the acquired differential gene set expression lists with a list of immune-related terms (Table S6). Statistical tests, graph plotting details and number of replicates are described in the figure legends for corresponding panels with CITE-seq data.

Loom files were generated from each batch (time point) of raw sequencing data using velocyto.py. To identify and subset cells of interest of velocity analysis, Seurat objects were converted into H5AD format. Cells of interest (cell type/time point) for velocity analysis were subset from the H5AD file and this list of cell identities was then used to subset the cells of interest from the loom file into an anndata object for analysis in SCANPY.[76] Metadata (including previously analyzed Seurat clustering plot points) for subset cells was merged into the subset anndata object. QC, filtering and normalization was performed on the subset anndata object with SCANPY. RNA velocity analysis was run on the subset anndata object following the scVelo pipeline using the velocity dynamical model.[38,39] Arrows generated through the velocity dynamical analysis were projected onto the Seurat cluster UMAP. High velocity genes were determined through scVelo rank_velocity_genes function.

Predicted subcluster trajectory analysis across time points was analyzed on subset anndata objects (described above) with the CellRank 2 RealTime kernel, employing the multi-omics single-cell optimal transport (moscot) framework.[40] The subset anndata objects were split by condition (vehicle- and ABX-treated) and processed through the RealTime analysis workflow (https://github.com/theislab/cellrank_notebooks/blob/main/tutorials/kernels/500_real_time.ipynb). The moscot method enables cells to be coupled across and within time points via optimal transport.[40] With the RealTime kernel, a cell-cell transition matrix is built which can be used for plotting and visualization of the flow of different cell subclusters between time points (displayed by vein plots in Figures 3 and 4).

Ligand-receptor interaction analysis was performed with NicheNetR following the "NicheNet analysis starting from a Seurat object" vignette.[43] Cells of interest (cell type and time point) were subset from Seurat objects and assigned as sender or receiver cells. Potential ligands of interest were extracted from sender cells depending on cognate receptor expression in the receiving cells. Ligand activity analysis was performed to identify top ligands based on the gene set of interest (differentially expressed genes in sender cells between two time points of interest). Target gene prediction was performed to infer regulatory potential of top ligands on gene expression changes occurring in sender cells.

CITE-seq data analyses were not performed blinded.

Supplementary Material

Refer to Web version on PubMed Central for supplementary material.

ACKNOWLEDGMENTS

This work was partially funded by NIH 1F31 CA261046-01 (to S.M.G.), a Walther Cancer Foundation Harper Cancer Research Institute award (to S.M.G.), NIH R01 CA194697-01 (to S.Z.), NIH R01 CA255064-01A1 (to S.Z.), NIH R21 CA263798-01 (to S.Z.), and the Cancer Prevention and Research Institute of Texas Scholar Award (to S.Z.). We thank the Dee Family endowment (to S.Z.) and are grateful for technical support from the following core facilities: Notre Dame Genomics and Bioinformatics Core Facility, Notre Dame Freimann Life Sciences Center, Indiana University School of Medicine Center for Medical Genomics, Indiana University Simon Cancer Center, Simmons Comprehensive Cancer Center, UT Southwestern (UTSW) Animal Resource Center, UTSW Microbiome Research Lab, UTSW Whole Brain Microscopy Facility, and UTSW BioHPC supercomputing facility.

REFERENCES

1. Quail DF, and Joyce JA (2017). The Microenvironmental Landscape of Brain Tumors. Cancer Cell 31, 326–341. 10.1016/j.ccell.2017.02.009. [PubMed: 28292436]
2. Doron H, Pukrop T, and Erez N (2019). A Blazing Landscape: Neuroinflammation Shapes Brain Metastasis. Cancer Res. 79, 423–436. 10.1158/0008-5472.CAN-18-1805. [PubMed: 30679177]
3. Ma W, Oliveira-Nunes MC, Xu K, Kossenkov A, Reiner BC, Crist RC, Hayden J, and Chen Q (2023). Type I interferon response in astrocytes promotes brain metastasis by enhancing monocytic myeloid cell recruitment. Nat. Commun. 14, 2632. 10.1038/s41467-023-38252-8. [PubMed: 37149684]
4. Priego N, Zhu L, Monteiro C, Mulders M, Wasilewski D, Bindeman W, Doglio L, Martínez L, Martínez-Saez E, Ramón Y Cajal S, et al. (2018). STAT3 labels a subpopulation of reactive astrocytes required for brain metastasis. Nat. Med. 24, 1024–1035. 10.1038/s41591-018-0044-4. [PubMed: 29892069]
5. Guldner IH, Wang Q, Yang L, Golomb SM, Zhao Z, Lopez JA, Brunory A, Howe EN, Zhang Y, Palakurthi B, et al. (2020). CNS-Native Myeloid Cells Drive Immune Suppression in the Brain

Metastatic Niche through Cxcl10. Cell 183, 1234–1248.e25. 10.1016/j.cell.2020.09.064. [PubMed: 33113353]

6. Bejarano L, Kauzlaric A, Lamprou E, Lourenco J, Fournier N, Ballabio M, Colotti R, Maas R, Galland S, Massara M, et al. (2024). Interrogation of endothelial and mural cells in brain metastasis reveals key immune-regulatory mechanisms. Cancer Cell 42, 378–395.e10. 10.1016/j.ccell.2023.12.018. [PubMed: 38242126]
7. Maas RR, Soukup K, Fournier N, Massara M, Galland S, Kornete M, Wischnewski V, Lourenco J, Croci D, Álvarez-Prado ÁF, et al. (2023). The local microenvironment drives activation of neutrophils in human brain tumors. Cell 186, 4546–4566.e27. 10.1016/j.cell.2023.08.043. [PubMed: 37769657]
8. Wu AML, Gossa S, Samala R, Chung MA, Gril B, Yang HH, Thorsheim HR, Tran AD, Wei D, Taner E, et al. (2021). Aging and CNS Myeloid Cell Depletion Attenuate Breast Cancer Brain Metastasis. Clin. Cancer Res. 27, 4422–4434. 10.1158/1078-0432.CCR-21-1549. [PubMed: 34083229]
9. Van Hove H, Martens L, Scheyltjens I, De Vlaminck K, Pombo Antunes AR, De Prijck S, Vandamme N, De Schepper S, Van Isterdael G, Scott CL, et al. (2019). A single-cell atlas of mouse brain macrophages reveals unique transcriptional identities shaped by ontogeny and tissue environment. Nat. Neurosci. 22, 1021–1035. 10.1038/s41593-019-0393-4. [PubMed: 31061494]
10. Keren-Shaul H, Spinrad A, Weiner A, Matcovitch-Natan O, Dvir-Szternfeld R, Ulland TK, David E, Baruch K, Lara-Astaiso D, Toth B, et al. (2017). A Unique Microglia Type Associated with Restricting Development of Alzheimer’s Disease. Cell 169, 1276–1290.e17. 10.1016/j.cell.2017.05.018. [PubMed: 28602351]
11. Mrdjen D, Pavlovic A, Hartmann FJ, Schreiner B, Utz SG, Leung BP, Lelios I, Heppner FL, Kipnis J, Merkler D, et al. (2018). High-Dimensional Single-Cell Mapping of Central Nervous System Immune Cells Reveals Distinct Myeloid Subsets in Health, Aging, and Disease. Immunity 48, 380–395.e6. 10.1016/j.immuni.2018.01.011. [PubMed: 29426702]
12. Jordão MJC, Sankowski R, Brendecke SM, Hagemeyer N, Locatelli G, Locatelli G, Tai YH, Tay TL, Schramm E, Armbruster S, et al. (2019). Single-cell profiling identifies myeloid cell subsets with distinct fates during neuroinflammation. Science 363, eaat7554. 10.1126/science.aat7554. [PubMed: 30679343]
13. Abdel-Haq R, Schlachetzki JCM, Glass CK, and Mazmanian SK (2019). Microbiome–microglia connections via the gut–brain axis. J. Exp. Med. 216, 41–59. 10.1084/jem.20180794. [PubMed: 30385457]
14. Sampson TR, and Mazmanian SK (2015). Control of Brain Development, Function, and Behavior by the Microbiome. Cell Host Microbe 17, 565–576. 10.1016/j.chom.2015.04.011. [PubMed: 25974299]
15. Ma Q, Xing C, Long W, Wang HY, Liu Q, and Wang R-F (2019). Impact of microbiota on central nervous system and neurological diseases: the gut-brain axis. J. Neuroinflammation 16, 53. 10.1186/s12974-019-1434-3. [PubMed: 30823925]
16. Fung TC, Olson CA, and Hsiao EY (2017). Interactions between the microbiota, immune and nervous systems in health and disease. Nat. Neurosci. 20, 145–155. 10.1038/nn.4476. [PubMed: 28092661]
17. Erny D, Hrabě de Angelis AL, Jaitin D, Wieghofer P, Staszewski O, David E, Keren-Shaul H, Mahlakoiv T, Jakobshagen K, Buch T, et al. (2015). Host microbiota constantly control maturation and function of microglia in the CNS. Nat. Neurosci. 18, 965–977. 10.1038/nn.4030. [PubMed: 26030851]
18. Erny D, Dokalis N, Mezö C, Castoldi A, Mossad O, Staszewski O, Frosch M, Villa M, Fuchs V, Mayer A, et al. (2021). Microbiota-derived acetate enables the metabolic fitness of the brain innate immune system during health and disease. Cell Metab. 33, 2260–2276.e7. 10.1016/j.cmet.2021.10.010. [PubMed: 34731656]
19. Rothhammer V, Borucki DM, Tjon EC, Takenaka MC, Chao C-C, Ardura-Fabregat A, de Lima KA, Gutiérrez-Vázquez C, Hewson P, Staszewski O, et al. (2018). Microglial control of astrocytes in response to microbial metabolites. Nature 557, 724–728. 10.1038/s41586-018-0119-x. [PubMed: 29769726]

20. Benakis C, Brea D, Caballero S, Faraco G, Moore J, Murphy M, Sita G, Racchumi G, Ling L, Pamer EG, et al. (2016). Commensal microbiota affects ischemic stroke outcome by regulating intestinal γδ T cells. Nat. Med. 22, 516–523. 10.1038/nm.4068. [PubMed: 27019327]
21. Khosravi A, Yáñez A, Price JG, Chow A, Merad M, Goodridge HS, and Mazmanian SK (2014). Gut Microbiota Promote Hematopoiesis to Control Bacterial Infection. Cell Host Microbe 15, 374–381. 10.1016/j.chom.2014.02.006. [PubMed: 24629343]
22. Zhang D, Chen G, Manwani D, Mortha A, Xu C, Faith JJ, Burk RD, Kunisaki Y, Jang J-E, Scheiermann C, et al. (2015). Neutrophil ageing is regulated by the microbiome. Nature 525, 528–532. 10.1038/nature15367. [PubMed: 26374999]
23. Buchta Rosean C, Bostic RR, Ferey JCM, Feng T-Y, Azar FN, Tung KS, Dozmorov MG, Smirnova E, Bos PD, and Rutkowski MR (2019). Pre-existing commensal dysbiosis is a host-intrinsic regulator of tissue inflammation and tumor cell dissemination in hormone receptor-positive breast cancer. Cancer Res. 79, 3662–3675. 10.1158/0008-5472.CAN-18-3464. [PubMed: 31064848]
24. Reikvam DH, Erofeev A, Sandvik A, Grcic V, Jahnsen FL, Gaustad P, McCoy KD, Macpherson AJ, Meza-Zepeda LA, and Johansen F-E (2011). Depletion of Murine Intestinal Microbiota: Effects on Gut Mucosa and Epithelial Gene Expression. PLoS One 6, e17996. 10.1371/journal.pone.0017996. [PubMed: 21445311]
25. Arpaia N, Campbell C, Fan X, Dikiy S, van der Veeken J, deRoos P, Liu H, Cross JR, Pfeffer K, Coffer PJ, and Rudensky AY (2013). Metabolites produced by commensal bacteria promote peripheral regulatory T-cell generation. Nature 504, 451–455. 10.1038/nature12726. [PubMed: 24226773]
26. Bachem A, Makhlouf C, Binger KJ, de Souza DP, Tull D, Hochheiser K, Whitney PG, Fernandez-Ruiz D, Dähling S, Kastenmüller W, et al. (2019). Microbiota-Derived Short-Chain Fatty Acids Promote the Memory Potential of Antigen-Activated CD8+ T Cells. Immunity 51, 285–297.e5. 10.1016/j.immuni.2019.06.002. [PubMed: 31272808]
27. Caetano-Silva ME, Rund L, Hutchinson NT, Woods JA, Steelman AJ, and Johnson RW (2023). Inhibition of inflammatory microglia by dietary fiber and short-chain fatty acids. Sci. Rep. 13, 2819. 10.1038/s41598-022-27086-x. [PubMed: 36797287]
28. Smith PM, Howitt MR, Panikov N, Michaud M, Gallini CA, Bohlooly-Y M, Glickman JN, and Garrett WS (2013). The Microbial Metabolites, Short-Chain Fatty Acids, Regulate Colonic Treg Cell Homeostasis. Science 341, 569–573. 10.1126/science.1241165. [PubMed: 23828891]
29. Tian Y, Xu Q, Sun L, Ye Y, and Ji G (2018). Short-chain fatty acids administration is protective in colitis-associated colorectal cancer development. J. Nutr. Biochem. 57, 103–109. 10.1016/j.jnutbio.2018.03.007. [PubMed: 29694938]
30. Park J, Kim M, Kang SG, Jannasch AH, Cooper B, Patterson J, and Kim CH (2015). Short-chain fatty acids induce both effector and regulatory T cells by suppression of histone deacetylases and regulation of the mTOR–S6K pathway. Mucosal Immunol. 8, 80–93. 10.1038/mi.2014.44. [PubMed: 24917457]
31. Trompette A, Gollwitzer ES, Pattaroni C, Lopez-Mejia IC, Riva E, Pernot J, Ubags N, Fajas L, Nicod LP, and Marsland BJ (2018). Dietary Fiber Confers Protection against Flu by Shaping Ly6c− Patrolling Monocyte Hematopoiesis and CD8+ T Cell Metabolism. Immunity 48, 992–1005.e8. 10.1016/j.immuni.2018.04.022. [PubMed: 29768180]
32. Bhaskaran N, Quigley C, Paw C, Butala S, Schneider E, and Pandiyan P (2018). Role of Short Chain Fatty Acids in Controlling Tregs and Immunopathology During Mucosal Infection. Front. Microbiol. 9, 1995. 10.3389/fmicb.2018.01995. [PubMed: 30197637]
33. Thion MS, Low D, Silvin A, Chen J, Grisel P, Schulte-Schrepping J, Blecher R, Ulas T, Squarzoni P, Hoeffel G, et al. (2018). Microbiome Influences Prenatal and Adult Microglia in a Sex-Specific Manner. Cell 172, 500–516.e16. 10.1016/j.cell.2017.11.042. [PubMed: 29275859]
34. Guldner IH, Golomb SM, Wang Q, Wang E, and Zhang S (2021). Isolation of mouse brain-infiltrating leukocytes for single cell profiling of epitopes and transcriptomes. STAR Protoc. 2, 100537. 10.1016/j.xpro.2021.100537. [PubMed: 34036283]
35. Stuart T, Butler A, Hoffman P, Hafemeister C, Papalexi E, Mauck WM, Hao Y, Stoeckius M, Smibert P, and Satija R (2019). Comprehensive Integration of Single-Cell Data. Cell 177, 1888–1902.e21. 10.1016/j.cell.2019.05.031. [PubMed: 31178118]

36. Hao Y, Stuart T, Kowalski MH, Choudhary S, Hoffman P, Hartman A, Srivastava A, Molla G, Madad S, Fernandez-Granda C, and Satija R (2024). Dictionary learning for integrative, multimodal and scalable single-cell analysis. Nat. Biotechnol. 42, 293–304. 10.1038/s41587-023-01767-y. [PubMed: 37231261]
37. Golomb SM, Guldner IH, Zhao A, Wang Q, Palakurthi B, Aleksandrovic EA, Lopez JA, Lee SW, Yang K, and Zhang S (2020). Multimodal Single-Cell Analysis Reveals Brain Immune Landscape Plasticity during Aging and Gut Microbiota Dysbiosis. Cell Rep. 33, 108438. 10.1016/j.celrep.2020.108438. [PubMed: 33264626]
38. La Manno G, Soldatov R, Zeisel A, Braun E, Hochgerner H, Petukhov V, Lidschreiber K, Kastriti ME, Lönnerberg P, Furlan A, et al. (2018). RNA velocity of single cells. Nature 560, 494–498. 10.1038/s41586-018-0414-6. [PubMed: 30089906]
39. Bergen V, Lange M, Peidli S, Wolf FA, and Theis FJ (2020). Generalizing RNA velocity to transient cell states through dynamical modeling. Nat. Biotechnol. 38, 1408–1414. 10.1038/s41587-020-0591-3. [PubMed: 32747759]
40. Weiler P, Lange M, Klein M, Pe’er D, and Theis F (2024). CellRank 2: unified fate mapping in multiview single-cell data. Nat. Methods 21, 1196–1205. 10.1038/s41592-024-02303-9. [PubMed: 38871986]
41. Mittnenzweig M, Mayshar Y, Cheng S, Ben-Yair R, Hadas R, Rais Y, Chomsky E, Reines N, Uzonyi A, Lumerman L, et al. (2021). A single-embryo, single-cell time-resolved model for mouse gastrulation. Cell 184, 2825–2842.e22. 10.1016/j.cell.2021.04.004. [PubMed: 33932341]
42. Gury-BenAri M, Thaiss CA, Serafini N, Winter DR, Giladi A, Lara-Astiaso D, Levy M, Salame TM, Weiner A, David E, et al. (2016). The Spectrum and Regulatory Landscape of Intestinal Innate Lymphoid Cells Are Shaped by the Microbiome. Cell 166, 1231–1246.e13. 10.1016/j.cell.2016.07.043. [PubMed: 27545347]
43. Browaeys R, Saelens W, and Saeys Y (2020). NicheNet: modeling intercellular communication by linking ligands to target genes. Nat. Methods 17, 159–162. 10.1038/s41592-019-0667-5. [PubMed: 31819264]
44. Vlaminck KD, Hove HV, Kancheva D, Scheyltjens I, Antunes ARP, Bastos J, Vara-Perez M, Ali L, Mampay M, Deneyer L, et al. (2022). Differential plasticity and fate of brain-resident and recruited macrophages during the onset and resolution of neuroinflammation. Immunity 55, 2085–2102.e9. 10.1016/j.immuni.2022.09.005. [PubMed: 36228615]
45. Evans KT, Blake K, Longworth A, Coburn MA, Insua-Rodríguez J, McMullen TP, Nguyen QH, Ma D, Lev T, Hernandez GA, et al. (2023). Microglia promote anti-tumour immunity and suppress breast cancer brain metastasis. Nat. Cell Biol. 25, 1848–1859. 10.1038/s41556-023-01273-y. [PubMed: 37957324]
46. de Graaf P, Mousson F, Geverts B, Scheer E, Tora L, Houtsmuller AB, and Timmers HTM (2010). Chromatin interaction of TATA-binding protein is dynamically regulated in human cells. J. Cell Sci. 123, 2663–2671. 10.1242/jcs.064097. [PubMed: 20627952]
47. Sherr CJ (1995). D-type cyclins. Trends Biochem. Sci. 20, 187–190. 10.1016/S0968-0004(00)89005-2. [PubMed: 7610482]
48. Fries GR, Gassen NC, and Rein T (2017). The FKBP51 Glucocorticoid Receptor Co-Chaperone: Regulation, Function, and Implications in Health and Disease. Int. J. Mol. Sci. 18, 2614. 10.3390/ijms18122614. [PubMed: 29206196]
49. Lempiäinen H, and Shore D (2009). Growth control and ribosome biogenesis. Curr. Opin. Cell Biol. 21, 855–863. 10.1016/j.ceb.2009.09.002. [PubMed: 19796927]
50. Fleming C, Cai Y, Sun X, Jala VR, Xue F, Morrissey S, Wei YL, Chien YH, Zhang HG, Haribabu B, et al. (2017). Microbiota-activated CD103 + DCs stemming from microbiota adaptation specifically drive γδT17 proliferation and activation. Microbiome 5, 46. 10.1186/s40168-017-0263-9. [PubMed: 28438184]
51. Sun M, Wu W, Chen L, Yang W, Huang X, Ma C, Chen F, Xiao Y, Zhao Y, Ma C, et al. (2018). Microbiota-derived short-chain fatty acids promote Th1 cell IL-10 production to maintain intestinal homeostasis. Nat. Commun. 9, 3555–3615. 10.1038/s41467-018-05901-2. [PubMed: 30177845]

52. Li W, Hang S, Fang Y, Bae S, Zhang Y, Zhang M, Wang G, McCurry MD, Bae M, Paik D, et al. (2021). A bacterial bile acid metabolite modulates Treg activity through the nuclear hormone receptor NR4A1. Cell Host Microbe 29, 1366–1377.e9. 10.1016/j.chom.2021.07.013. [PubMed: 34416161]

53. Alves de Lima K, Rustenhoven J, Da Mesquita S, Wall M, Salvador AF, Smirnov I, Martelossi Cebinelli G, Mamuladze T, Baker W, Papadopoulos Z, et al. (2020). Meningeal γδ T cells regulate anxiety-like behavior via IL-17a signaling in neurons. Nat. Immunol. 21, 1421–1429. 10.1038/s41590-020-0776-4. [PubMed: 32929273]

54. Ma Y, Aymeric L, Locher C, Mattarollo SR, Delahaye NF, Pereira P, Boucontet L, Apetoh L, Ghiringhelli F, Casares N, et al. (2011). Contribution of IL-17–producing γδ T cells to the efficacy of anticancer chemotherapy. J. Exp. Med. 208, 491–503. 10.1084/jem.20100269. [PubMed: 21383056]

55. Coffelt SB, Kersten K, Doornebal CW, Weiden J, Vrijland K, Hau C-S, Verstegen NJM, Ciampricotti M, Hawinkels LJAC, Jonkers J, and de Visser KE (2015). IL-17-producing γδ T cells and neutrophils conspire to promote breast cancer metastasis. Nature 522, 345–348. 10.1038/nature14282. [PubMed: 25822788]

56. Jin C, Lagoudas GK, Zhao C, Bullman S, Bhutkar A, Hu B, Ameh S, Sandel D, Liang XS, Mazzilli S, et al. (2019). Commensal Microbiota Promote Lung Cancer Development via γδ T Cells. Cell 176, 998–1013.e16. 10.1016/j.cell.2018.12.040. [PubMed: 30712876]

57. Koenecke C, Chennupati V, Schmitz S, Malissen B, Förster R, and Prinz I (2009). In vivo application of mAb directed against the γδ TCR does not deplete but generates "invisible" γδ T cells. Eur. J. Immunol. 39, 372–379. 10.1002/eji.200838741. [PubMed: 19130484]

58. Rosenblum MD, Way SS, and Abbas AK (2016). Regulatory T cell memory. Nat. Rev. Immunol. 16, 90–101. 10.1038/nri.2015.1. [PubMed: 26688349]

59. Mundt S, Mrdjen D, Utz SG, Greter M, Schreiner B, and Becher B (2019). Conventional DCs sample and present myelin antigens in the healthy CNS and allow parenchymal T cell entry to initiate neuroinflammation. Sci. Immunol. 4, eaau8380. 10.1126/sciimmunol.aau8380. [PubMed: 30679199]

60. Willis EF, and Vukovic J (2020). Protocol for brain-wide or region-specific microglia depletion and repopulation in adult mice. STAR Protoc. 1, 100211. 10.1016/j.xpro.2020.100211. [PubMed: 33377105]

61. Vance RE, Jamieson AM, and Raulet DH (1999). Recognition of the Class Ib Molecule Qa-1b by Putative Activating Receptors Cd94/Nkg2c and Cd94/Nkg2e on Mouse Natural Killer Cells. J. Exp. Med. 190, 1801–1812. [PubMed: 10601355]

62. Lohwasser S, Kubota A, Salcedo M, Lian RH, and Takei F (2001). The non-classical MHC class I molecule Qa-1b inhibits classical MHC class I-restricted cytotoxicity of cytotoxic T lymphocytes. Int. Immunol. 13, 321–327. 10.1093/intimm/13.3.321. [PubMed: 11222501]

63. Suvas S, Azkur AK, and Rouse BT (2006). Qa-1b and CD94-NKG2a Interaction Regulate Cytolytic Activity of Herpes Simplex Virus-Specific Memory CD8+ T Cells in the Latently Infected Trigeminal Ganglia1. J. Immunol. 176, 1703–1711. 10.4049/jimmunol.176.3.1703. [PubMed: 16424200]

64. André P, Denis C, Soulas C, Bourbon-Caillet C, Lopez J, Arnoux T, Bléry M, Bonnafous C, Gauthier L, Morel A, et al. (2018). Anti-NKG2A mAb Is a Checkpoint Inhibitor that Promotes Anti-tumor Immunity by Unleashing Both T and NK Cells. Cell 175, 1731–1743.e13. 10.1016/j.cell.2018.10.014. [PubMed: 30503213]

65. Blay J-Y, and von Mehren M (2011). Nilotinib: a Novel, Selective Tyrosine Kinase Inhibitor. Semin. Oncol. 38, S3–S9. 10.1053/j.seminoncol.2011.01.016.

66. de Visser KE, and Joyce JA (2023). The evolving tumor microenvironment: From cancer initiation to metastatic outgrowth. Cancer Cell 41, 374–403. 10.1016/j.ccell.2023.02.016. [PubMed: 36917948]

67. Chen H, Nwe P-K, Yang Y, Rosen CE, Bielecka AA, Kuchroo M, Cline GW, Kruse AC, Ring AM, Crawford JM, and Palm NW (2019). A Forward Chemical Genetic Screen Reveals Gut Microbiota Metabolites That Modulate Host Physiology. Cell 177, 1217–1231.e18. 10.1016/j.cell.2019.03.036. [PubMed: 31006530]

68. Tanoue T, Morita S, Plichta DR, Skelly AN, Suda W, Sugiura Y, Narushima S, Vlamakis H, Motoo I, Sugita K, et al. (2019). A defined commensal consortium elicits CD8 T cells and anti-cancer immunity. Nature 565, 600–605. 10.1038/s41586-019-0878-z. [PubMed: 30675064]
69. Baruch EN, Youngster I, Ben-Betzalel G, Ortenberg R, Lahat A, Katz L, Adler K, Dick-Necula D, Raskin S, Bloch N, et al. (2021). Fecal microbiota transplant promotes response in immunotherapy-refractory melanoma patients. Science 371, 602–609. 10.1126/science.abb5920. [PubMed: 33303685]
70. Postler TS, and Ghosh S (2017). Understanding the Holobiont: How Microbial Metabolites Affect Human Health and Shape the Immune System. Cell Metab. 26, 110–130. 10.1016/j.cmet.2017.05.008. [PubMed: 28625867]
71. Cullin N, Azevedo Antunes C, Straussman R, Stein-Thoeringer CK, and Elinav E (2021). Microbiome and cancer. Cancer Cell 39, 1317–1341. 10.1016/j.ccell.2021.08.006. [PubMed: 34506740]
72. Schindelin J, Arganda-Carreras I, Frise E, Kaynig V, Longair M, Pietzsch T, Preibisch S, Rueden C, Saalfeld S, Schmid B, et al. (2012). Fiji: an open-source platform for biological-image analysis. Nat. Methods 9, 676–682. 10.1038/nmeth.2019. [PubMed: 22743772]
73. Ihaka R, and Gentleman R (1996). R: A Language for Data Analysis and Graphics. J. Comput. Graph Stat. 5, 299–314. 10.1080/10618600.1996.10474713.
74. Satija R, Farrell JA, Gennert D, Schier AF, and Regev A (2015). Spatial reconstruction of single-cell gene expression data. Nat. Biotechnol. 33, 495–502. 10.1038/nbt.3192. [PubMed: 25867923]
75. Hänzelmann S, Castelo R, and Guinney J (2013). GSVA: gene set variation analysis for microarray and RNA-seq data. BMC Bioinf. 14, 7. 10.1186/1471-2105-14-7.
76. Wolf FA, Angerer P, and Theis FJ (2018). SCANPY: large-scale single-cell gene expression data analysis. Genome Biol. 19, 15. 10.1186/s13059-017-1382-0. [PubMed: 29409532]
77. Callahan BJ, McMurdie PJ, Rosen MJ, Han AW, Johnson AJA, and Holmes SP (2016). DADA2: High-resolution sample inference from Illumina amplicon data. Nat. Methods 13, 581–583. 10.1038/nmeth.3869. [PubMed: 27214047]

Highlights

- ABX-induced gut dysbiosis is associated with increased brain metastasis outgrowth
- Ly6C$^+$ monocytes exhibit an asynchronous inflammatory response
- Inflammatory microglia are enriched in ABX-treated mice at late-stage brain metastasis
- T cells and microglia regulate brain metastasis outgrowth under conditions of gut dysbiosis

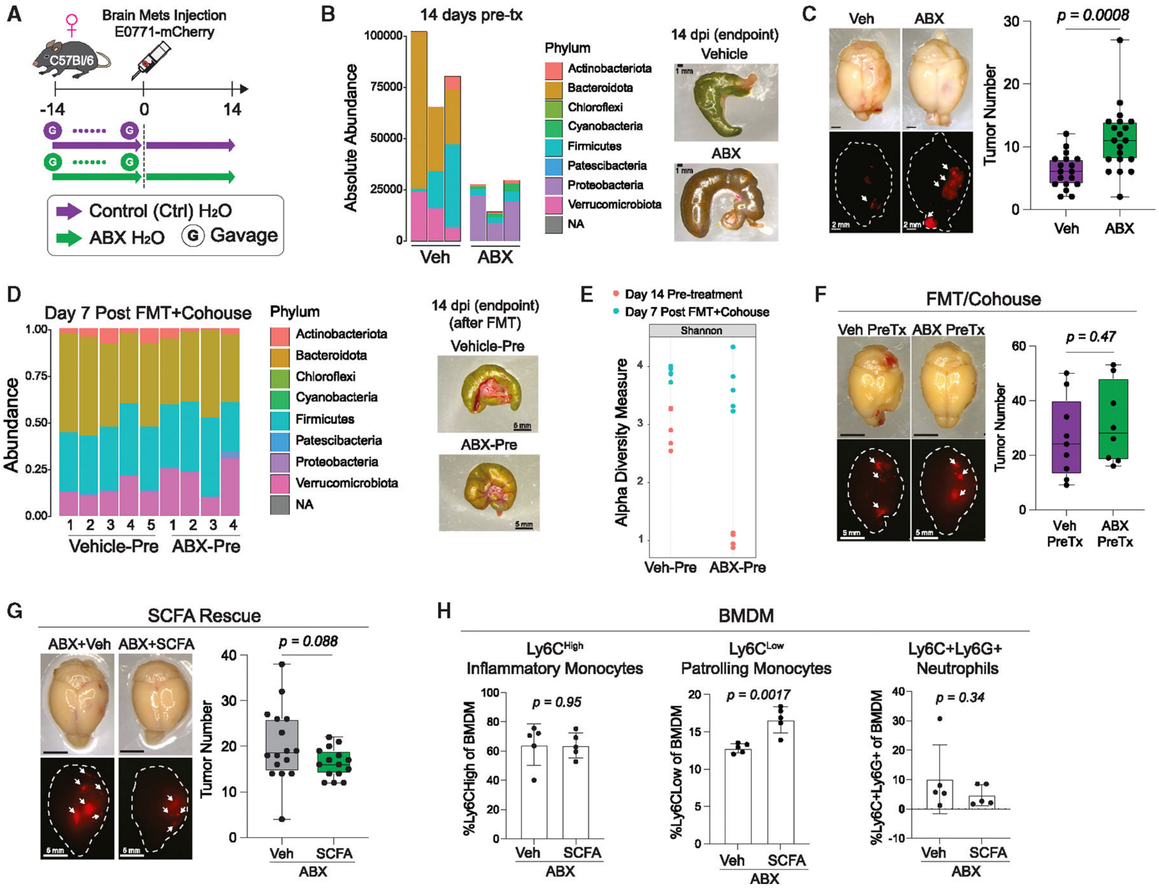

Figure 1. ABX-induced gut dysbiosis is associated with increased BrMet burden.

(A) Experimental BrMet with vehicle and ABX treatment.

(B) Bacterial phylum absolute abundance measured by 16S rRNA-seq (left) and stereoscope images of ceca from vehicle- or ABX-treated mice at the endpoint (right). Scale bar: 1 mm. Three biological replicates per group.

(C) Stereoscope images of BrMet (left) and quantification of tumor number in vehicle- and ABX-treated mice (quantification based on pooled data from two independent experiments with ≥8 mice per group) (right). Scale bar: 2 mm.

(D) Bacterial phylum abundance frequency post FMT and cohousing measured by 16S rRNA-seq (each bar represents 1 mouse) (left) and stereoscope images of ceca with vehicle or ABX pre-tx and FMT/cohousing at the endpoint (right).

(E) Alpha diversity measured by Shannon's diversity index after 14-day vehicle or ABX pre-tx and 7 days following FMT/cohousing.

(F) Stereoscope images of BrMet from FMT/cohoused vehicle- and ABX-pre-treated mice (left) and quantification of tumor number in each group (right).

(G) Stereoscope images of BrMet from vehicle+ABX- and SCFA+ABX-treated mice (left) and quantification of tumor number in each group (quantification based on pooled data from two independent experiments with ≥6 mice per group) (right).

(H) Percentages of the indicated immune populations in vehicle- or SCFA-supplemented BrMet-burdened brains from enriched brain immune cells, measured by flow cytometry.

Data in (C) and (F)–(H) were analyzed with two-tailed Student’s t test. Scale bars: 5 mm (G) and (H). Each dot represents 1 mouse in (C) and (E)–(H). Error bars in (F) and (G) represent minimum (min) and maximum (max), and center represents mean. Error bars in (H) represent SD. See also Figure S1.

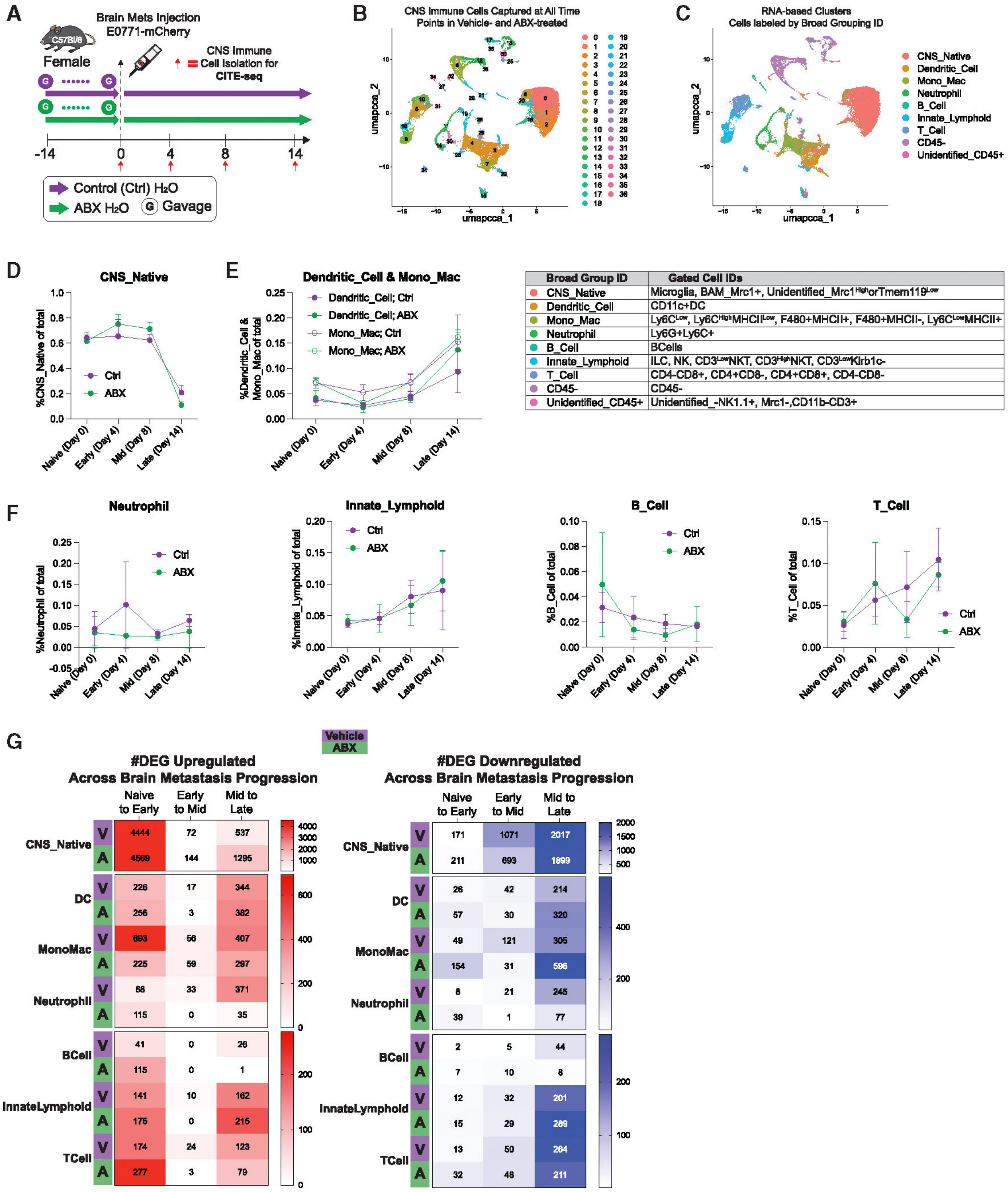

	Broad Group ID	Gated Cell IDs
●	CNS_Native	Microglia, BAM_Mrc1+, Unidentified_Mrc1^{High}orTmem119^{Low}
●	Dendritic_Cell	CD11c+DC
●	Mono_Mac	Ly6C^{Low}, Ly6C^{High}MHCII^{Low}, F480+MHCII+, F480+MHCII-, Ly6C^{Low}MHCII+
●	Neutrophil	Ly6G+Ly6C+
●	B_Cell	BCells
●	Innate_Lymphoid	ILC, NK, CD3^{Low}NKT, CD3^{High}NKT, CD3^{Low}Klrb1c-
●	T_Cell	CD4-CD8+, CD4+CD8-, CD4+CD8+, CD4-CD8-
●	CD45-	CD45-
●	Unidentified_CD45+	Unidentified_-NK1.1+, Mrc1-,CD11b-CD3+

#DEG Upregulated Across Brain Metastasis Progression

		Naive to Early	Early to Mid	Mid to Late
CNS_Native	V	4444	72	537
	A	4569	144	1295
DC	V	226	17	344
	A	256	3	382
MonoMac	V	693	56	407
	A	225	59	297
Neutrophil	V	68	33	371
	A	115	0	35
BCell	V	41	0	26
	A	115	0	1
InnateLymphoid	V	141	10	162
	A	175	0	215
TCell	V	174	24	123
	A	277	3	79

#DEG Downregulated Across Brain Metastasis Progression

		Naive to Early	Early to Mid	Mid to Late
CNS_Native	V	171	1071	2017
	A	211	693	1899
DC	V	26	42	214
	A	57	30	320
MonoMac	V	49	121	305
	A	154	31	596
Neutrophil	V	8	21	245
	A	39	1	77
BCell	V	2	5	44
	A	7	10	8
InnateLymphoid	V	12	32	201
	A	15	29	289
TCell	V	13	50	264
	A	32	48	211

Figure 2. CITE-seq delineates dynamics of the brain immune environment in BrMet in mice with or without gut dysbiosis.

(A) Experimental approach for CITE-seq.

(B and C) UMAP of merged cells from all time points and conditions colored by (B) transcriptional cluster ID and (C) broad grouping ID (top) with assigned gated cell ID to broad cell grouping ID (bottom).

(D–F) Percentage of broad group of total cells at each time point and condition for (D) CNS_Native, (E) Dendritic_Cell and Mono_Mac, and (F) Neutrophil, Innate_Lymphoid, B_Cell, and T_Cell.

(G) Heatmap of the total number of significant DEGs upregulated (left) and downregulated (right) for each broad grouping ID across each time point and condition. All plots were derived from pooling three biological replicates per time point and condition. Error bars in (D)–(F) represent SD. DEGs in (G) were analyzed by Wilcoxon rank-sum test. See also Figures S1 and S2, and Tables S1–S4.

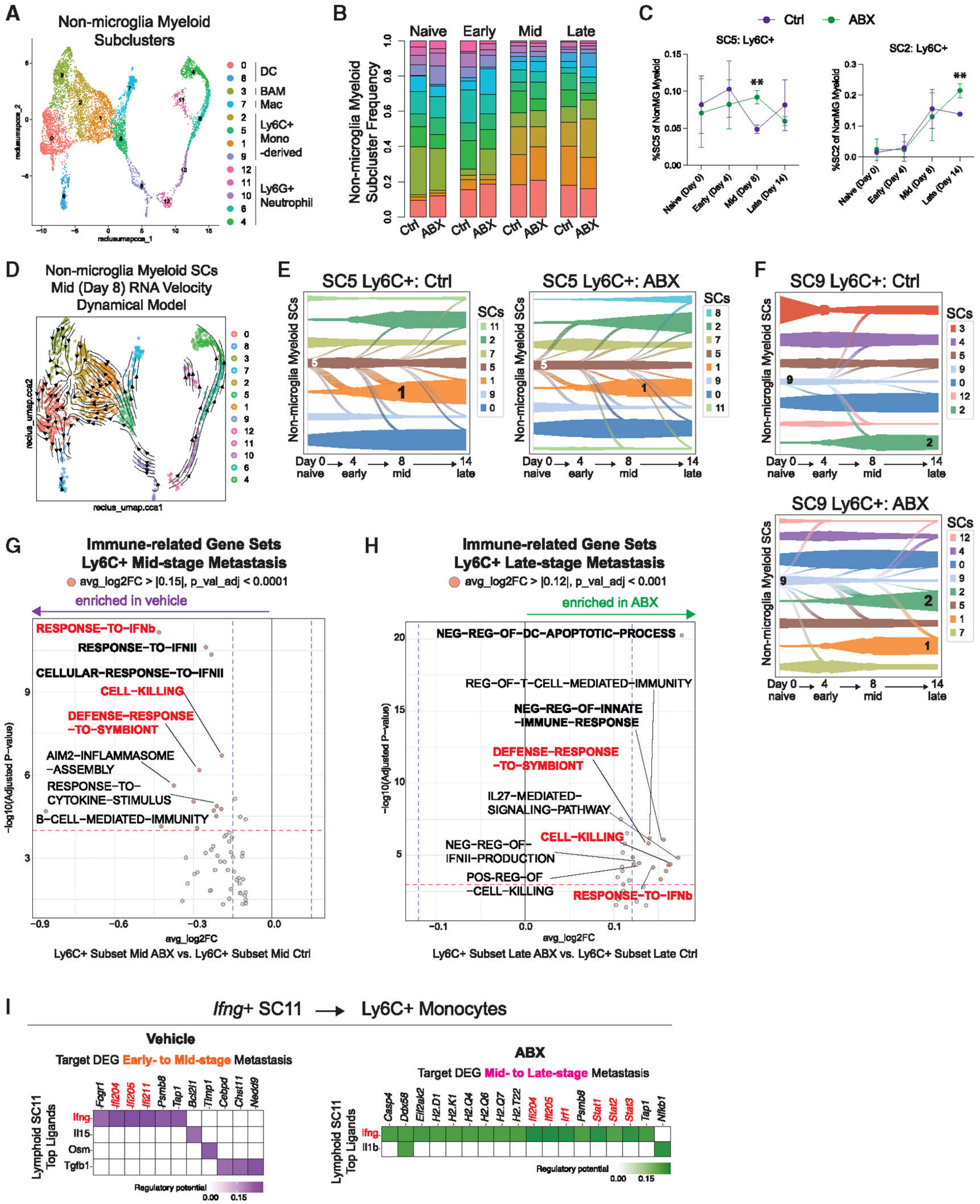

Figure 3. *Ly6c2*$^{+}$ monocyte response diverges with ABX treatment.

(A) UMAP of reclustered NonMGMyeloids (Table S4), colored by transcriptional SCs.

(B) Stacked bar charts of the percentages of NonMGMyeloid SCs at each time point and condition.

(C) Percentages of NonMGMyeloid SC5 (left) and NonMGMyeloid SC2 (right) of NonMGMyeloids at each time point and condition.

(D) UMAP of NonMGMyeloids from mid-stage (day 8) overlaid with RNA velocity arrows (dynamic model). Cells are colored by transcriptional SCs.

(E and F) Vein plots describing continuous transition of cell types to direct descendants and showing the flow of NonMGMyeloid SCs emanating from (E) SC5 in control (Ctrl) (left) and ABX (right) and (F) SC9 in Ctrl (top) and ABX (bottom) across time.

(G and H) Volcano plot of immune-related differentially expressed gene sets (DEGS) in the Ly6C monocyte subset between ABX- and vehicle-treated mice at (G) mid-stage and (H) late-stage.

(I) Top-predicted lymphoid SC11 ligands with ≥0.2 regulatory potential on early- to mid-stage DEGs in Ly6C$^+$ monocytes in vehicle-treated (left) and mid- to late-stage DEGs in Ly6C$^+$ monocytes in ABX-treated mice (right).

All plots were derived from pooling three biological replicates per time point and condition. Data in (C) were analyzed by two-tailed Student's t test; error bars represent SD. Data in (G) and (H) were analyzed by Wilcoxon rank-sum test. See also Figures S3 and S4 and Tables S2, S3, S5, and S6.

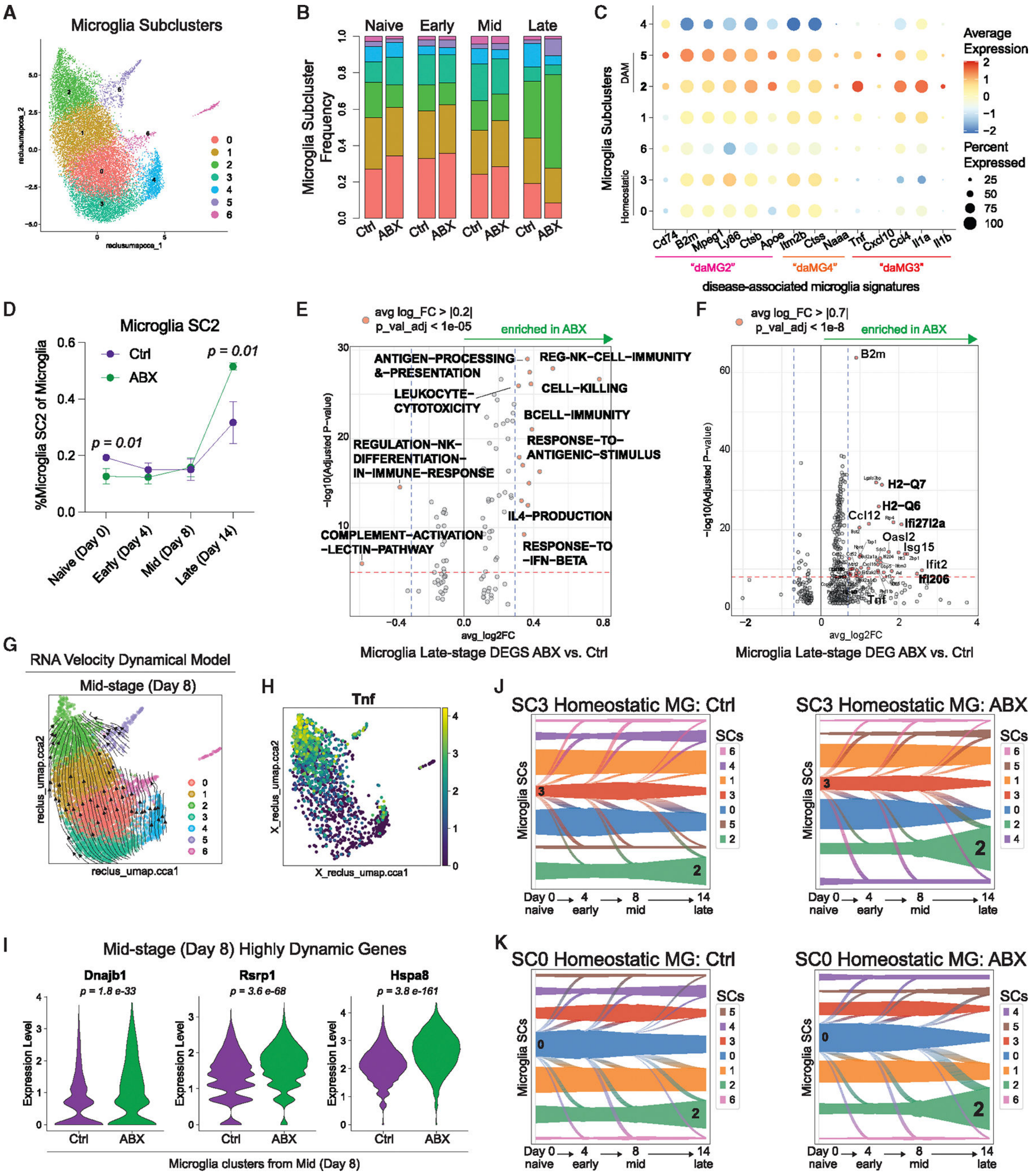

Figure 4. Tnf^{High} inflammatory microglia are enriched in late-stage BrMet in mice with gut dysbiosis.

(A) UMAP of the reclustered microglia subset (Table S4), colored by transcriptional SCs.

(B) Stacked bar charts of the percentage of microglia SCs at each time point and condition.

(C) Dot plot of relative gene expression levels (color scale) and percentages (dot size) for daMGs in microglia SCs.

(D) Percentage of microglia SC2 of the microglia subset at each time point and condition.

(E and F) Volcano plots of (E) immune-related DEGS and (F) DEGs in the microglia subset between ABX- and vehicle-treated mice at late-stage.

(G) UMAP of the microglia subset from mid-stage overlaid with RNA velocity arrows (dynamic model). Cells are colored by transcriptional SCs.

(H) UMAP of microglia subset from late-stage with cells colored by relative expression of *Tnf*.

(I) Violin plots of expression of highly dynamic genes at mid-stage in the microglia subset from mid-stage.

(J and K) Vein plot showing the flow of microglia SCs emanating from (J) SC3 in Ctrl (left) and ABX (right) and (K) SC0 in Ctrl (left) and ABX (right) across time. All plots were derived from pooling three biological replicates per time point and condition. Data in (D) were analyzed by two-tailed Student's t test; error bars represent SD. Data in (E) and (F) and DEGs in (I) were analyzed by Wilcoxon rank-sum test. See also Figures S4 and S5 and Tables S2, S3, S6, and S7.

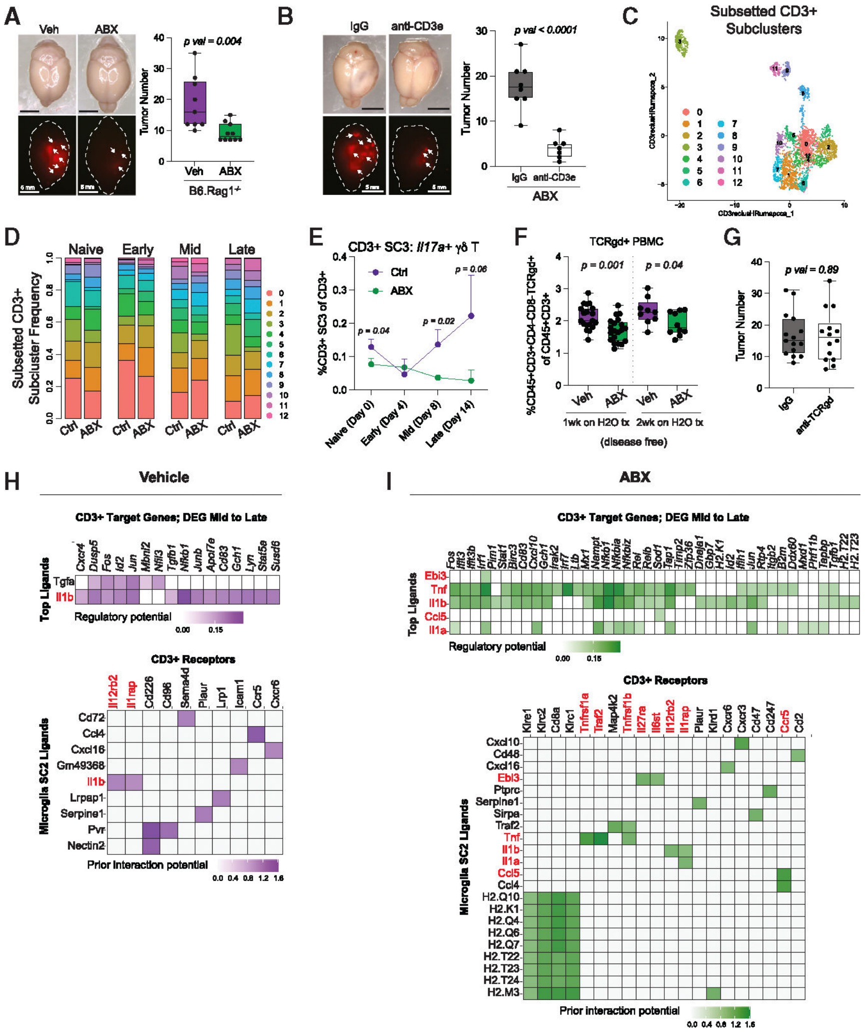

Figure 5. T cells impact BrMet outgrowth under ABX conditions.

(A) Stereoscope images of BrMet in brains of *B6.Rag1*$^{-/-}$ vehicle- and ABX-treated mice (left) and quantification of tumor number in each group (right).

(B) Stereoscope images of BrMet in brains of ABX-treated mice with IgG or anti-CD3e treatment (left) and quantification of tumor number in each group (right).

(C) UMAP of the reclustered CD3^{+} T cell subset, colored by transcriptional SCs.

(D) Stacked bar charts of the percentages of CD3+ T cell SCs at each time point and condition.

(E) Percentage of CD3^{+} T cell SC3: *Il17a*$^{+}$ γδ T cells of the CD3^{+} T cell subset at each time point and condition.

(F) Percentage of TCRgd^{+} T cells among T cells in circulation after 1 and 2 weeks of vehicle and ABX treatment, measured by flow cytometry (quantification based on pooled data from four independent experiments with ≥4 mice per group).

(G) Brain tumor quantification of IgG- and anti-TCRgd-treated mice (quantification based on pooled data from two independent experiments with ≥4 mice per group).

(H and I) Top predicted microglia SC2 ligands with ≥0.06 regulatory potential on mid- to late-stage DEGs in the CD3^{+} T cell subset (top) and ≥0.9 interaction potential with expressed receptors in the CD3$^+$ T cell subset (bottom) in (H) vehicle-treated and (I) ABX-treated mice.

In (A), (B), (F), and (G) each dot represents 1 mouse. Data were analyzed with two-tailed Student's t test, error bars represent min and max, and center represents mean. Scale bars: 5 mm (A) and (B). Data in (E) were analyzed with two-tailed Student's t test, and error bars represent SD. Plots in (C)–(E), (H), and (I) were derived from pooling three biological replicates per time point and condition. See also Figure S6 and Tables S2 and S3.

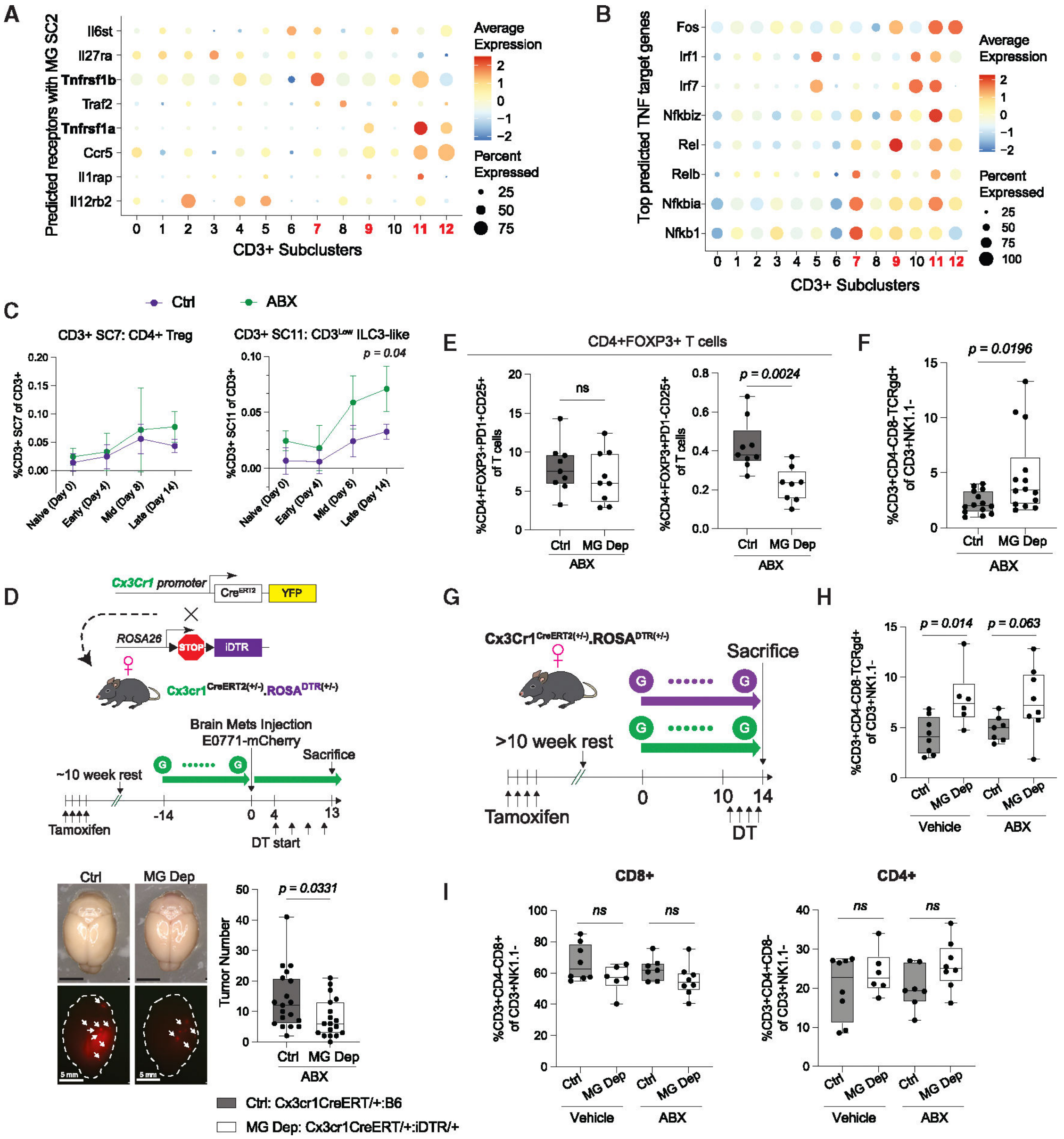

Figure 6. MGDep is associated with decreased BrMet and shifting of PD1$^-$ Tregs and γδ T cells under ABX conditions.

(A and B) Dot plot of the relative gene expression level for (A) predicted receptors in the CD3$^+$ T cell subset for interaction with top predicted ligands in microglia SC2 and (B) top predicted Tnf target genes in the CD3$^+$ T cell subset.

(C) Percentages of CD3$^+$ SC7: CD4$^+$ Tregs (left) and CD3$^+$ SC11: CD3^{Low} ILC3-like (right) of the CD3$^+$ T cell subset at each time point and condition.

(D) Schematic for MGDep and ABX treatment (top), stereoscope images of BrMet in control or MGDep mice on ABX treatment (left), and quantification of tumor number in each group (quantification based on pooled data from two independent experiments with ≥8 mice per group) (right). Scale bar: 5 mm.

(E and F) Percentages (E) of the indicated CD4$^+$FOXP3$^+$ and (F) TCRgd$^+$ T cell populations in control and MGDep BrMet-burdened brains.

(G) Schematic of MGDep and vehicle/ABX treatment in tumor-naive mice.

(H and I) Percentages (H) of the TCRgd$^+$ and (I) CD8$^+$ (left) and CD4$^+$ (right) T cell populations in control and MGDep tumor-naive brains in vehicle- and ABX-treated mice. Plots in (A)–(C) were derived from pooling three biological replicates per time point and condition. Dot plots in (A) and (B) have relative gene expression level depicted by color scale and percentage by dot size. Data in (C) were analyzed with two-tailed Student's t test, and error bars represent SD. Each dot represents 1 mouse in (D)–(F), (H), and (I), with data analyzed by two-tailed Student's t test, error bars representing min and max, and center representing mean. Immune cells in (E), (F), (H), and (I) were enriched from brain tissue and measured by flow cytometry. See also Figures S6 and S7 and Tables S2 and S3.

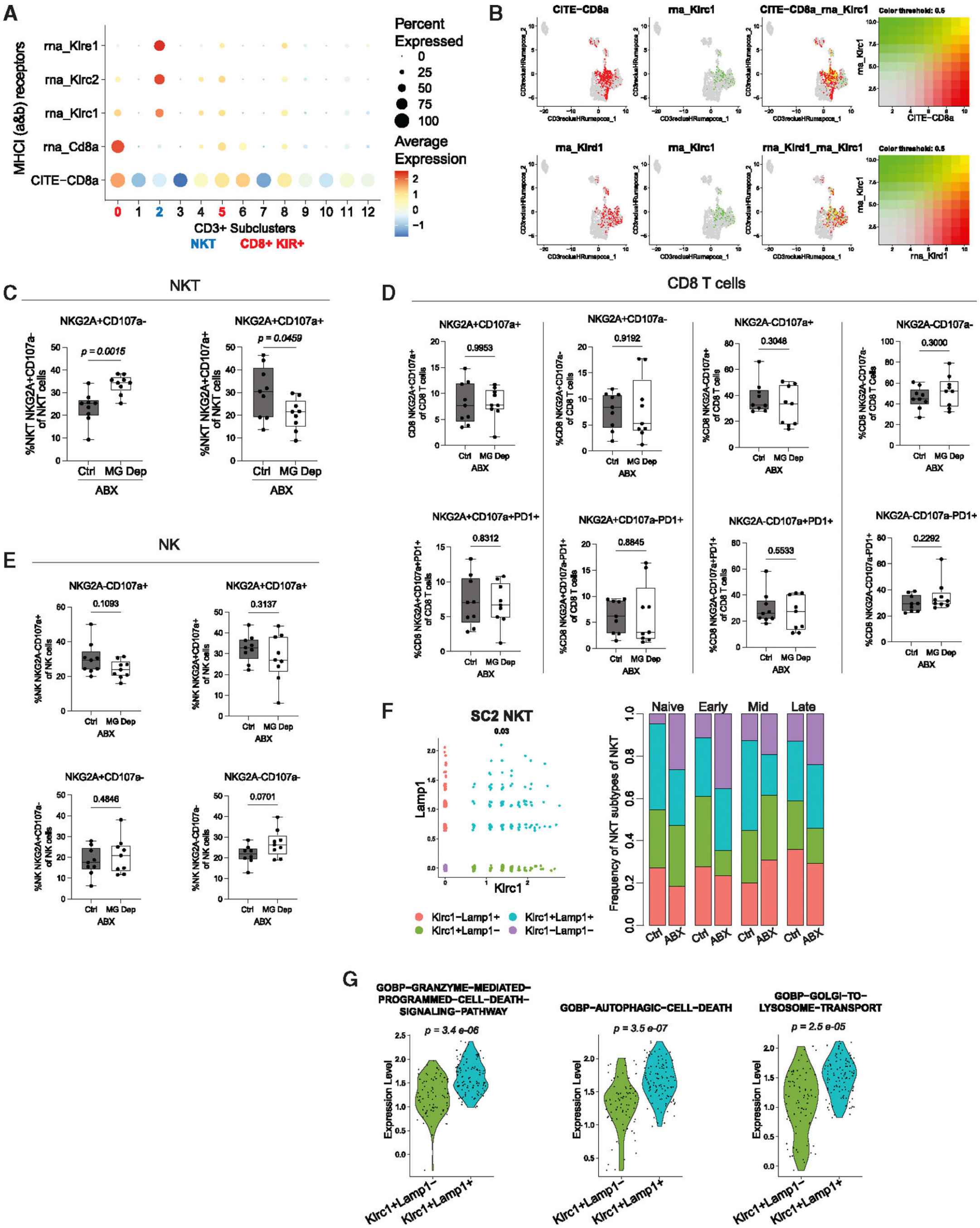

Figure 7. NK T cell subsets are altered with MGDep and ABX treatment in BrMet-burdened brains.

(A) Dot plot of the relative gene expression level of predicted MHCI receptors across CD3$^+$ T cell SCs. Relative gene expression level is depicted by color scale and percentage by dot size.

(B) Feature plots showing cells in the CD3$^+$ T cell subset with co-expression of CD8 (top) and Klrd1 (bottom) with Klrc1.

(C–E) Percentages of the indicated (C) NK T cell, (D) CD8 T cell, and (E) NK cell populations in control and MGDep BrMet-burdened brains.

(F) Biaxial plot depicting the CD3$^+$ SC2: NK T cell subset with and without *Klrc1* and *Lamp1* gene expression (left) and stacked bar charts of NK T cell subsets at each time point and condition (right).

(G) Violin plot of DEGS on subset NK T cell populations.

Plots in (A), (B), (F), and (G) were derived from pooling three biological replicates per time point and condition. Each dot represents 1 mouse in (C)–(E), with data analyzed by two-tailed Student’s t test, error bars representing min and max, and center representing mean. Immune cells in (C)–(E) were enriched from brain tissue and measured by flow cytometry. Data in (G) were analyzed by Wilcoxon rank-sum test. See also Figure S7 and Tables S2 and S6.

KEY RESOURCES TABLE

REAGENT or RESOURCE	SOURCE	IDENTIFIER
Antibodies		
CITE-seq: rat anti-CCR2/CD192 (SA203G11)	Biolegend	Cat#150625; RRID:AB_2783122
CITE-seq: rat anti-CD117/c-kit (2B8)	Biolegend	Cat#105843; RRID:AB_2749960
CITE-seq: rat anti-CD11b (M1/70)	Biolegend	Cat#101265; RRID:AB_2734152
CITE-seq: armenian hamster anti-CD11c (N418)	Biolegend	Cat#117355; RRID:AB_2750352
CITE-seq: rat anti-CD172a/SIRPα (P84)	Biolegend	Cat#144033; RRID:AB_2800670
CITE-seq: rat anti-CD25 (PC61)	Biolegend	Cat#102055; RRID:AB_2749982
CITE-seq: rat anti-CD3 (17A2)	Biolegend	Cat#100251; RRID:AB_2750533
CITE-seq: rat anti-CD38 (90)	Biolegend	Cat#102733; RRID:AB_2750556
CITE-seq: rat anti-CD4 (RM4–5)	Biolegend	Cat#100569; RRID:AB_2749956
CITE-seq: rat anti-CD44 (IM7)	Biolegend	Cat#103045; RRID:AB_2734154
CITE-seq: rat anti-CD45 (30-F11)	Biolegend	Cat#103159; RRID:AB_2734156
CITE-seq: rat anti-CD45R/B220 (RA3–6B2)	Biolegend	Cat#103263; RRID:AB_2734158
CITE-seq: rat anti-CD86 (GL-1)	Biolegend	Cat#105047; RRID:AB_2750348
CITE-seq: rat anti-CD8a (53–6.7)	Biolegend	Cat#100773; RRID:AB_2734151
CITE-seq: mouse anti-CD90.1 (OX-7)	Biolegend	Cat#202547; RRID:AB_2783141
CITE-seq: mouse anti-Cx3cr1 (SA011F11)	Biolegend	Cat#149041; RRID:AB_2783121
CITE-seq: rat anti-F4/80 (BM8)	Biolegend	Cat#123153; RRID:AB_2749986
CITE-seq: rat anti-I-A/I-E (M5/114.15.2)	Biolegend	Cat#107653; RRID:AB_2750505
CITE-seq: rat anti-Ly6C (HK1.4)	Biolegend	Cat#128047; RRID:AB_2749961

REAGENT or RESOURCE	SOURCE	IDENTIFIER
CITE-seq: rat anti-Ly6G (1A8)	Biolegend	Cat#127655; RRID:AB_2749962
CITE-seq: mouse anti-NK1.1 (PK136)	Biolegend	Cat#108755; RRID:AB_2750536
CITE-seq: rat anti-PD-1 (RMP1–30)	Biolegend	Cat#109123; RRID:AB_2734169
CITE-seq: rat anti-PD-L1 (MIH6)	Biolegend	Cat#153604; RRID:AB_2783125
CITE-seq: rat anti-CD169/Siglec-1 (3D6.112)	Biolegend	Cat#142425; RRID:AB_2783106
CITE-seq: rat anti-Siglec-H (551)	Biolegend	Cat#129615; RRID:AB_275053
CITE-seq: mouse anti-TMEM119 (A16075D)	Biolegend	Cat#853303; RRID:AB_2801201
CITE-seq: mouse anti-XCR1 (Zet)	Biolegend	Cat#148227; RRID:AB_2783120
CITE-seq: rat anti-CD24 (M1/69)	Biolegend	Cat#101841; RRID:AB_2750380
CITE-seq: rat armenian hamster anti-CD103 (2e7)	Biolegend	Cat#121437; RRID:AB_2750349
CITE-seq: mouse anti-CD64 (X54–5/7.1)	Biolegend	Cat#139325; RRID:AB_2750367
CITE-seq: mouse anti-CD83 (Michel-19)	Biolegend	Cat#121519; RRID:AB_2783061
CITE-seq: rat anti-mouse Hashtag 1 antibody (M1/42; 30-F11)	Biolegend	Cat#155801; RRID:AB_2750032
CITE-seq: rat anti-mouse Hashtag 2 antibody (M1/42; 30-F11)	Biolegend	Cat#155803; RRID:AB_2750033
CITE-seq: rat anti-mouse Hashtag 3 antibody (M1/42; 30-F11)	Biolegend	Cat#155805; RRID:AB_2750034
CITE-seq: rat anti-mouse Hashtag 4 antibody (M1/42; 30-F11)	Biolegend	Cat#155807; RRID:AB_2750035
CITE-seq: rat anti-mouse Hashtag 5 antibody (M1/42; 30-F11)	Biolegend	Cat#155809; RRID:AB_2750036
CITE-seq: rat anti-mouse Hashtag 6 antibody (M1/42; 30-F11)	Biolegend	Cat#155811; RRID:AB_2750037
Flow: rat anti-mouse CD3e-Alexa Fluor 647 (KT3.1.1)	BioLegend	Cat#155609; RRID:AB_2750435
Flow: hamster anti-mouse TCR g/day-PE (GL3)	BioLegend	Cat#118107; RRID: AB_313831
Flow: rat anti-mouse CD117(c-kit)-PE-Cy7 (2B8)	BioLegend	Cat#105813; RRID: AB_313222
Flow: mouse anti-mouse CX3CR1-Brilliant Violet 421 (SA011F11)	BioLegend	Cat#149023; RRID: AB_2565706
Flow: rat anti-mouse CD192(CCR2)-Brilliant Violet 510 (SA203G11)	BioLegend	Cat#150617; RRID: AB_2721535
Flow: rat anti-mouse CD3-Spark Blue 550 (17A2)	BioLegend	Cat#100259; RRID: AB_2819767
Flow: rat anti-mouse CD8-FITC (53–6.7)	BioLegend	Cat#100706; RRID: AB_312744

REAGENT or RESOURCE	SOURCE	IDENTIFIER
Flow: rat anti-mouse CD4-Brilliant Violet 711 (RM4–5)	BioLegend	Cat#100549; RRID: AB_2562099
Flow: rat anti-mouse Ly-6C-Brilliant Violet 785 (HK1.4)	BioLegend	Cat#128041; RRID: AB_2565852
Flow: rat anti-mouse Ly-6G-Brilliant Violet 650 (1A8)	BioLegend	Cat#127641; RRID: AB_2565881
Flow: rat anti-mouse CD186 (CXCR6)-PerCP/Cyanine5.5 (SA051D1)	BioLegend	Cat#151120; RRID: AB_2888878
Flow: rat anti-mouse CD11b-Brilliant Violet 605 (M1/70)	BioLegend	Cat#101237; RRID: AB_11126744
Flow: rat anti-mouse CD45-Pacific Blue (30-F11)	BioLegend	Cat#103125; RRID: AB_493535
Flow: rat anti-mouse CD45-PerCP/Cyanine5.5 (30-F11)	BioLegend	Cat#103131; RRID: AB_893340
Flow: rat anti-CD3-FITC (17A2)	BioLegend	Cat#100203; RRID: AB_312661
Flow: hamster anti-mouse TCR g/day-PE-Cy7 (GL3)	BioLegend	Cat#118123; RRID: AB_11203530
Flow: rat anti-mouse CD279(PD-1)-Brilliant Violet 421 (29F.1A12)	BioLegend	Cat#135217; RRID: AB_2561447
Flow: rat anti-CD25-PE (PC61)	BioLegend	Cat#102007; RRID: AB_312856
Flow: rat anti-CD4-APC-Cy7 (RM4–5)	Tonbo	Cat#25–0042-U025; RRID: N/A
Flow: rat anti-mouse CD8a-red Flour 710 (53–6.7)	Tonbo	Cat#80–0081-U025; RRID: N/A
Flow: rat anti-mouse CD3-Pacific Blue (17A2)	BioLegend	Cat#100213; RRID: AB_493644
Flow: rat anti-mouse CD4-Brilliant Violet 570 (RM4–5)	BioLegend	Cat#100541; RRID: AB_10897943
Flow: rat anti-mouse CD8a-APC-Cy7 (53–6.7)	BioLegend	Cat#100713; RRID: AB_312752
Flow: hamster anti-mouse TCR g/day-Brilliant Violet 711 (GL3)	BioLegend	Cat#118149; RRID: AB_3083110
Flow: mouse anti-mouse NK-1.1-Spark Red 718 (S17016D)	BioLegend	Cat#156533; RRID: AB_2924486
Flow: rat anti-mouse CD25-Brilliant Violet 750 (PC61)	BioLegend	Cat#102077; RRID: AB_3068099
Flow: mouse anti-mouse CD159a(NKG2A^{B6})-PE (16A11)	BioLegend	Cat#142803; RRID: AB_10959654
Flow: rat anti-mouse CD107a(LAMP-1)-PE-Cy7 (1D4B)	BioLegend	Cat#121619; RRID: AB_2562146
Flow: rat anti-mouse/human CD11b-Brilliant Violet 650 (M1/70)	BioLegend	Cat#101259; RRID: AB_11125575
Flow: rat anti-mouse CD8a-Alexa Fluor 647 (53–6.7)	BioLegend	Cat#100727; RRID: AB_389326
Flow: rat anti-mouse CD279(PD-1)-421 (29F.1A12)	BioLegend	Cat#135221; RRID: AB_2561447
Flow: rat anti-mouse FOXP3-Alexa Fluor 647 (MF-14)	BioLegend	Cat#126407; RRID: AB_1089115
In vivo TX: hamster anti-mouse CD3e (145–2C11)	BioXCell	Cat# BE0001–1; RRID: AB_1107634

REAGENT or RESOURCE	SOURCE	IDENTIFIER
In vivo TX: hamster IgG (polyclonal)	BioXCell	Cat#BE0091; RRID: AB_1107773
In vivo TX: hamster anti-mouse TCRg/d (UC7–13D5)	BioXCell	Cat#BE0070; RRID: AB_1107751
In vivo TX: mouse anti-mouse/rat IL-17A (17F3)	BioXCell	Cat#BE0173; RRID: AB_10950102
In vivo TX: mouse IgG1 (MOPC-21)	BioXCell	Cat#BE0083; RRID: AB_1107784
IF: guinea pig anti-TMEM119 (polyclonal)	Synaptic Systems	Cat#400–004; RRID: AB_2744645
IF: Alexa Fluor 594 AffiniPure Donkey Anti-Guinea Pig IgG (H + L)	Jackson Immuno Research	Cat#706–585-148; RRID: AB_2340474
IF: Alexa Fluor 488 AffiniPure Donkey Anti-Guinea Pig IgG (H + L)	Jackson Immuno Research	Cat#706–545-148; RRID: AB_2340472
Chemicals, peptides, and recombinant proteins		
FcR Block Reagent, mouse	Miltenyi Biotec	Cat#130–092-575, RRID: N/A
metronidazole	MedChem Express	Cat#HY-B0318
vancomycin hydrochloride	MedChem Express	Cat#HY-17362
ampicillin sodium salt	Fisher Scientific	Cat#BP1760–5
Neomycin sulfate	VWR	Cat#0558
sodium propionate	Sigma-Aldrich	Cat#P1880
sodium butyrate	Sigma-Aldrich	Cat#B5887
sodium acetate	MP Biomedicals	Cat#02195496.5
Tamoxifen	Sigma	Cat#T5648
Diphtheria Toxin	Sigma	Cat#D0564
percoll	Cytiva	Cat#17089101
Hanks Balanced Salt Solution (HBSS), 1x, -Ca, -Mg, Phenol Red	Cytiva	Cat#SH30588.01
red blood cell lysis buffer	Tonbo	Cat# TNB-4300-L100
DAPI	Biotium	Cat#40043
Critical commercial assays		
ZombieAqua Fixable Viability Kit	BioLegend	Cat#423102; RRID: N/A
Multi-tissue Dissociation Kit I	Miltenyi Biotec	Cat#130–110-201; RRID: N/A
Chromium Single Cell 30 Library and Gel Bead Kit v3	10x Genomics	Cat# PN-10000092; RRID: N/A
Chromium Next GEM Single Cell 30 GEM Library and Gel Bead Kit v3.1	10x Genomics	Cat# PN-1000121; RRID: N/A
Chromium Chip B Single Cell Kit	10x Genomics	Cat# PN-1000074; RRID: N/A
Chromium i7 Multiplex Kit	10x Genomics	Cat# PN-120262; RRID: N/A

REAGENT or RESOURCE	SOURCE	IDENTIFIER
ZymoBIOMICS DNA Miniprep Kit	Zymo Research	Cat#D4300; RRID: N/A
Nextera XT Index Kit	Illumina	Cat#FC-131–1096; RRID: N/A
True-Nuclear Transcription Factor Buffer Set	BioLegend	Cat#424401; RRID: N/A
Deposited data		
Mouse CITE-seq data	This paper	GSE270629
Mouse 16S rRNA sequencing data	This paper	GSE270809
Experimental models: Cell lines		
E0771	CH3 Biosystems	SKU:940001-Vial, RRID: N/A
E0771.Br	Guldner et al.[5]	Dr. Siyuan Zhang, RRID: N/A
Experimental models: Organisms/strains		
C57BL/6	Jackson Laboratories	Stock#:000664; RRID: N/A
B6.129P2(Cg)-Cx3cr1$^{tm2.1(cre/ERT2)Litt/WganJ}$	Jackson Laboratories	Stock#:021160; RRID: N/A
C57BL/6-Gt(ROSA)26^{Sortm1}(HBEGF)$^{Awai/J}$	Jackson Laboratories	Stock#:007900; RRID: N/A
B6.129S7-Rag1^{tm1Mom}/J	Jackson Laboratories	Stock#:002216; RRID: N/A
B6.129(Cg)-Ccr2$^{tm2.1Ifc/J}$	Jackson Laboratories	Stock#:017586; RRID: N/A
Oligonucleotides		
ADT_TruSeq_i7_UDI01: CAAGCAGAAGACGGCATACGAGAACCGCGGGTGACTGGAGTTCCTTGGCACCCGAGAATTCCA	This paper	N/A
HTO_Nextera_i7_UDP01: CAAGCAGAAGACGGCATACGAGATCGCTCAGTGTGACTGGAGTTCAGACGTGTG	This paper	N/A
ADT-RPI-2: CAAGCAGAAGACGGCATACGAGATCGTGATGTGACTGGAGTTCCTTGGCACCCGAGAATTCCA	This paper	N/A
HTO_Nextera_i7_UDP01: CAAGCAGAAGACGGCATACGAGATCGCTCAGTGTGACTGGAGTTCAGACGTGTG	This paper	N/A
ADT_TruSeq_i7_UDI04: CAAGCAGAAGACGGCATACGAGTTGGACTTGTGACTGGAGTTCCTTGGCACCCGAGAATTCCA	This paper	N/A
HTO_ Nextera_i7_UDP02: CAAGCAGAAGACGGCATACGAGATTATCTGACGTGACTGGAGTTCAGACGTGTGC	This paper	N/A

REAGENT or RESOURCE	SOURCE	IDENTIFIER
ADT-RPI-1: CAAGCAGAAGACGGCATACG AGATCGTGATGTGACTGGAGTTCCTTGG CACCCGAGAATTCCA	This paper	N/A
HTO-N701: CAAGCAGAAGACGGCATACG AGATTCGCCTTAGTGACTGGAGTTCAGA CGTGTGC	This paper	N/A
Software and algorithms		
FlowJo	BD	https://www.flowjo.com
Fiji	Schindelin et al.[72]	https://fiji.sc/
R Studio	Ihaka and Gentleman[73]	https://rstudio.com
CellRanger 7.2	10x Genomics	https://www.10xgenomics.com/support/software/cell-ranger/latest
GraphPad Prism	GraphPad Software	https://www.graphpad.com
Seurat v5	Satija et al.[74]	https://satijalab.org/seurat/
GSVA	Hanzelmann et al.[75]	https://rdrr.io/bioc/GSVA/
RNA Velocity	La Manno et al.[38]	http://velocyto.org
CellRank 2	Weiler et al.[40]	https://cellrank.readthedocs.io/en/latest/index.html
SCANPY	Wolf et al.[76]	https://scanpy.readthedocs.io/en/stable/
NicheNet	Browaeys et al.[43]	https://nichenet.be
Divisive Amplicon Denoising Algorithm version 2 (DADA2)	Callahan et al.[77]	https://benjjneb.github.io/dada2/
Other		
Beckman Coulter FC500	Beckman Coulter	N/A
Cytek Northen Lights/SpectroFlo	Cytek Biosciences	N/A
Illumina NovaSeq 6000	Illumina	N/A
Illumina MiSeq	Illumina	N/A
Leica M165 FC fluorescence stereoscope	Leica Biosystems	N/A
Nikon Ti2	Nikon	N/A
10x Chromium Controller and Accessory Kit	10x Genomics	N/A